



1 Data Processing Algorithms for Generating Textured 3D Building Facade 2 Meshes from Laser Scans and Camera Images

3 CHRISTIAN FRUEH, SIDDHARTH JAIN AND AVIDEH ZAKHOR

4 *Video and Image Processing Laboratory, Department of Electrical Engineering and Computer Sciences,*
5 *University of California, Berkeley*

6 frueh@eecs.berkeley.edu

7 morpheus@eecs.berkeley.edu

8 avz@eecs.berkeley.edu

9 *Received May 29, 2003; Revised April 9, 2004; Accepted April 9, 2004*

10 *First online version published in October, 2004*

11 **Abstract.** In this paper, we develop a set of data processing algorithms for generating textured facade meshes of
12 cities from a series of vertical 2D surface scans and camera images, obtained by a laser scanner and digital camera
13 while driving on public roads under normal traffic conditions. These processing steps are needed to cope with
14 imperfections and non-idealities inherent in laser scanning systems such as occlusions and reflections from glass
15 surfaces. The data is divided into easy-to-handle quasi-linear segments corresponding to approximately straight
16 driving direction and sequential topological order of vertical laser scans; each segment is then transformed into a
17 depth image. Dominant building structures are detected in the depth images, and points are classified into foreground
18 and background layers. Large holes in the background layer, caused by occlusion from foreground layer objects,
19 are filled in by planar or horizontal interpolation. The depth image is further processed by removing isolated points
20 and filling remaining small holes. The foreground objects also leave holes in the texture of building facades, which
21 are filled by horizontal and vertical interpolation in low frequency regions, or by a copy-paste method otherwise.
22 We apply the above steps to a large set of data of downtown Berkeley with several million 3D points, in order to
23 obtain texture-mapped 3D models.

24 **Keywords:** 3D city model, occlusion, hole filling, image restoration, texture synthesis, urban simulation

25 1. Introduction

26 Three-dimensional models of urban environments are
27 useful in a variety of applications such as urban
28 planning, training and simulation for urban terrorism
29 scenarios, and virtual reality. Currently, the standard
30 technique for creating large-scale city models in an au-
31 tomated or semi-automated way is to use stereo vi-
32 sion approaches on aerial or satellite images (Frere
33 et al., 1998; Kim et al., 2001). In recent years, ad-
34 vances in resolution and accuracy of airborne laser
35 scanners have also rendered them suitable for the gener-
36 ation of reasonable models (Haala and Brenner, 1997;

Maas, 2001). Both approaches have the disadvantage 37
that their resolution is only in the range of 1 to 2 feet, 38
and more importantly, they can only capture the roofs 39
of the buildings but not the facades. This essential dis- 40
advantage prohibits their use in photo realistic walk or 41
drive-through applications. 42

There exist a number of approaches to acquire the 43
complementary ground-level data and to reconstruct 44
building facades; however, these approaches are 45
typically limited to one or few buildings. Debevec 46
et al. (1996) propose to reconstruct buildings based 47
on few camera images in a semi-automated way. Dick 48
et al. (2001), Koch et al. (1999), and Wang et al. 49

50 (2002) apply automated vision-based techniques for
 51 localization and model reconstruction, but varying
 52 lighting conditions, the scale of the environment, and
 53 the complexity of outdoor scenes with many trees and
 54 glass surfaces generally pose enormous challenges to
 55 purely vision-based methods.

56 Stamos and Allen (2002) use a 3D laser scanner and
 57 Thrun et al. (2000) use 2D laser scanners mounted on
 58 a mobile robot to achieve complete automation, but the
 59 time required for data acquisition of an entire city is
 60 prohibitively large; in addition, the reliability of au-
 61 tonomous mobile robots in outdoor environments is
 62 a critical issue. In Zhao and Shibasaki (1999), use a
 63 vertical laser scanner mounted on a van, which is lo-
 64 calized by using odometry, an inertial navigation sys-
 65 tem, and the Global Positioning System (GPS), and
 66 thus with limited accuracy. While GPS is by far the
 67 most common source of global position estimates in
 68 outdoor environments, even expensive high-end Dif-
 69 ferential GPS systems become inaccurate or erroneous
 70 in urban canyons where there are not enough satellites
 71 in a direct line of sight.

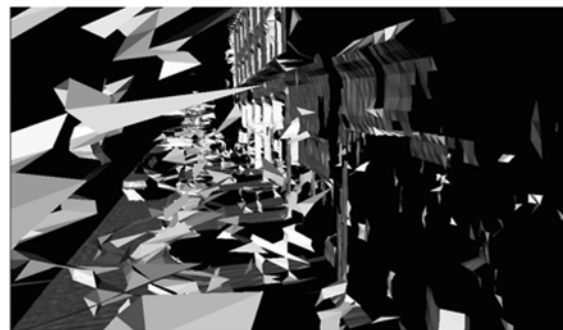
72 In previous work, we have developed a fast, auto-
 73 mated data acquisition system capable of acquiring
 74 3D geometry and texture data for an entire city at the
 75 ground level by using a combination of a horizontal
 76 and a vertical 2D laser scanners and a digital camera
 77 (Frueh et al., 2001; Frueh and Zakhor, 2001a). This sys-
 78 tem is mounted on a truck, moving at normal speeds on
 79 public roads, collecting data to be processed offline. It
 80 is similar to the one independently proposed by Zhao
 81 and Shibasaki (2001), which also use 2D laser scanners
 82 in horizontal and vertical configuration; however, our
 83 system differs from that of Zhao and Shibasaki (2001)
 84 in that we use a normal camera instead of a line cam-
 85 era. Both approaches have the advantage that data can

86 be acquired continuously, rather than in a stop-and-
 87 go fashion, and are thus extremely fast; relative posi-
 88 tion changes are computed with centimeter accuracy
 89 by matching successive horizontal laser scans against
 90 each other. In Frueh and Zakhor (2001b), we proposed
 91 to use the particle-filtering-based Monte-Carlo Local-
 92 ization (Fox et al., 2000) to correct accumulating pose
 93 uncertainty by using airborne data such as an aerial
 94 photo or a digital surface model (DSM) as a map. An
 95 advantage of our approach is that both scan points and
 96 camera images are registered with airborne data, facil-
 97 itating a subsequent fusion with models derived from
 98 this data (Frueh and Zakhor, 2003).

99 In this paper, we describe our approach to processing
 100 the globally registered scan points and camera images
 101 obtained in our ground-based data acquisition, and to
 102 creating detailed, textured 3D facade models. As there
 103 are many erroneous scan points, e.g. due to glass sur-
 104 faces, and foreground objects partially occluding the
 105 desired buildings, the generation of a facade mesh is
 106 not straightforward. A simple triangulation of the raw
 107 scan points by connecting neighboring points whose
 108 distance is below a threshold value does not result
 109 in an acceptable reconstruction of the street scenery,
 110 as shown in Figs. 1(a) and (b). Even though the 3D
 111 structure can be easily recognized when viewed from
 112 a viewpoint near the original acquisition position as in
 113 Fig. 1(a), the mesh appears cluttered due to several rea-
 114 sons; first, there are holes and erroneous vertices due
 115 to reflections off the glass on windows; second, there
 116 are pieces of geometry “floating in the air”, correspond-
 117 ing to partially captured objects or measurement errors.
 118 The mesh appears to be even more problematic when
 119 viewed from other viewpoints such as the one shown in
 120 Fig. 1(b); this is because in this case the large holes in
 the building facades caused by occluding foreground



(a)



(b)

Figure 1. Triangulated raw points: (a) front view; (b) side view.

121 objects, such as cars and trees, become entirely visi-
 122 ble. Furthermore, since the laser scan only captures the
 123 frontal view of foreground objects, they become almost
 124 unrecognizable when viewed sideways. As we drive by
 125 a street only once, it is not possible to use additional
 126 scans from other viewpoints to fill in gaps caused by
 127 occlusions, as is done in Curless and Levoy (1996) and
 128 Stamos and Allen (2002). Rather, we have to recon-
 129 struct occluded areas by using cues from neighboring
 130 scan points; as such, there has been little work to solve
 131 this problem (Stulp et al., 2001).

132 In this paper, we propose a class of data processing
 133 techniques to create visually appealing facade meshes
 134 by removing noisy foreground objects and filling holes
 135 in the geometry and texture of building facades. Our
 136 objectives are robustness and efficiency with regards
 137 to processing time, in order to ensure scalability to the
 138 enormous amount of data resulting from a city scan.
 139 The outline of this paper is as follows: In Section 2, we
 140 introduce our data acquisition system and position esti-
 141 mation; Section 3 discusses data subdivision and depth
 142 image generation schemes. We describe our strategy to
 143 transform the raw scans into a visually appealing fa-
 144 cade mesh in Sections 4 through 6; Section 7 discusses
 145 foreground and background segmentation of images,
 146 automatic texture atlas generation, and texture synthe-
 147 sis. The experimental results are presented in Section 8.

148 2. Data acquisition and Position Estimation

149 As described in Frueh et al. (2001) and Frueh and
 150 Zakhor (2001a), we have developed a data acquisition
 151 system consisting of two Sick LMS 2D laser scanners,
 152 and a digital color camera with a wide-angle lens. As



Figure 2. Truck with data acquisition equipment.

153 seen in Fig. 2, this system is mounted on a rack approx-
 154 imately 3.6 meters high on top of a truck, in order to
 155 obtain measurements that are not obstructed by pedes-
 156 trians and cars. The scanners have a 180° field of view
 157 with a resolution of 1°, a range of 80 meters and an
 158 accuracy of ± 3.5 centimeters. Both 2D scanners face
 159 the same side of the street and are mounted at a 90-
 160 degree angle. The first scanner is mounted vertically
 161 with the scanning plane orthogonal to the driving di-
 162 rection, and scans the buildings and street scenery as
 163 the truck drives by. The data captured by this scanner
 164 is used for reconstructing 3D geometry as described
 165 in this paper. The second scanner is mounted horizon-
 166 tally and is used for determining the position of the
 167 truck for each vertical scan. Finally, the digital camera
 168 is used to acquire the appearance of the scanned build-
 169 ing facades. It is oriented in the same direction as the
 170 scanners, with its center of projection approximately
 171 in the intersection line of the two scanning planes. All
 172 three devices are synchronized with each other using
 173 hardware-generated signals, and their coordinate sys-
 174 tems are calibrated with respect to each other prior to
 175 the acquisition. Thus, we obtain long series of vertical
 176 scans, horizontal scans and camera images that are all
 177 associated with each other.

178 We introduce a Cartesian world coordinate system
 179 $[x, y, z]$ where x, y is the ground plane and z points
 180 into the sky. While our truck performs a 6 degree-
 181 of-freedom motion, its primary motion components
 182 are x, y , and θ (yaw), i.e. its two-dimensional (2D)
 183 motion. As described in detail in Frueh and Zakhor
 184 (2001a), we reconstruct the driven path and determine
 185 the global pose for each scan by using the horizontal
 186 laser scanner: First, an estimate of the 2D relative pose
 187 $(\Delta x, \Delta y, \Delta \theta)$ between each pair of subsequent scans is
 188 obtained via scan-to-scan matching; these relative esti-
 189 mates are concatenated to form a preliminary estimate
 190 for the driven path. Then, in order to correct the global
 191 pose error resulting from accumulation of error due to
 192 relative estimates, we utilize an aerial image or a DSM
 193 as a global map, and apply Monte-Carlo-Localization
 194 (Frueh and Zakhor, 2001b). Matching ground-based
 195 horizontal laser scans with edges in the global map, we
 196 track the vehicle and correct the preliminary path ac-
 197 cordingly to obtain a globally registered 2D trajectory
 198 as shown in Fig. 3. As described in Frueh and Zakhor
 199 (2003), we obtain the secondary motion components
 200 z and pitch by utilizing the altitude information pro-
 201 vided by the DSM, and the roll motion by correlating
 202 subsequent camera images, respectively.

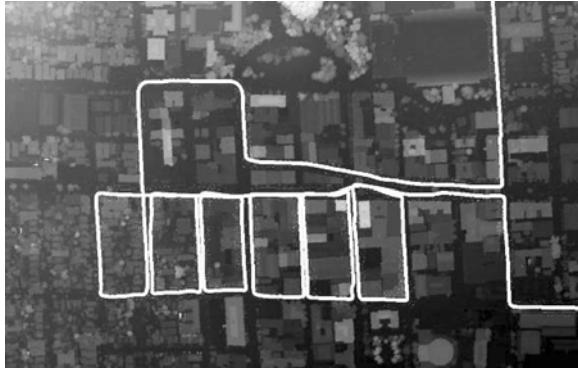


Figure 3. Driven path superimposed on top of a DSM.

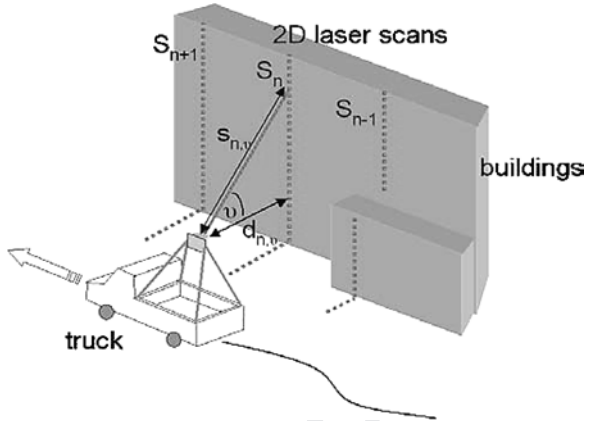


Figure 4. Scanning setup.

203 While we use the full 6 degree-of-freedom pose to
 204 compute the final x, y, z coordinates of each scan point
 205 in the final model, we can for convenience and sim-
 206 plicity neglect the 3 secondary motion components for
 207 most of the intermediate processing steps described in
 208 the following sections of this paper. Furthermore, to re-
 209 duce the amount of required processing and to partially
 210 compensate for the unpredictable, non-uniform speed
 211 of the truck, we do not utilize all the scans captured
 212 during slow motion; rather, we subsample the series of
 213 vertical scans such that the spacing between succes-
 214 sive scans is roughly equidistant. Thus, in our process-
 215 ing steps described in this paper, we assume the scan
 216 data to be given as a series of roughly equally spaced
 217 vertical scans S_n with an associated tuple (x_n, y_n, θ_n)
 218 describing 2D position and orientation of the scanner
 219 in the world coordinate system during acquisition. Fur-
 220 thermore, we use $s_{n,v}$ to denote the distance measure-
 221 ment on a point in scan S_n with azimuth angle ν , and
 222 $d_{n,v} = \cos(\nu) \cdot s_{n,v}$ to denote the depth value of this
 223 point with respect to the scanner, i.e. its orthogonal
 224 projection into the ground plane, as shown in Fig. 4.

225 3. Data Subdivision and Depth Image Generation

226 3.1. Segmentation of the Driving Path into Quasi 227 Linear Segments

228 The captured data during a 20-minute drive consists
 229 of tens of thousands of vertical scan columns. Since
 230 successive scans in time correspond to spatially close
 231 points, e.g. a building or a side of a street block, it is
 232 computationally advantageous not to process the entire
 233 data as one block, rather to split it into smaller segments
 234 to be processed separately. We impose the constraints

that (a) path segments have low curvature, and (b) scan
 235 columns have a regular grid structure. This allows us
 236 to readily identify the neighbors to right, left, above
 237 and below for each point, and, as seen later, is essential
 238 for the generation of a depth image and segmentation
 239 operations. 240

Scan points for each truck position are obtained as
 241 we drive by the streets. During straight segments, the
 242 spatial order of the 2D scan rows is identical to the
 243 temporal order of the scans, forming a regular topol-
 244 ogy. Unfortunately, this order of scan points can be
 245 reversed during turns towards the scanner side of the
 246 car. Figure 5(a) and (b) show the scanning setup dur-
 247 ing such a turn, with scan planes indicated by the two
 248 dotted rays. During the two vertical scans, the truck per-
 249 forms not only a translation but also a rotation, making
 250 the scanner look slightly backwards during the second
 251 scan. If the targeted object is close enough, as shown in
 252 Fig. 5(a), the spatial order of scan points 1 and 2 is still
 253 the same as the temporal order of the scans; however,
 254 if the object is further away than a critical distance d_{crit} ,
 255 the spatial order of the two scan points is reversed, as
 256 shown in Fig. 5(b). 257

For a given truck translation of Δs , and a rotation
 258 $\Delta \theta$ between successive scans, the critical distance can
 259 be computed as 260

$$d_{crit} = \frac{\Delta s}{\sin(\Delta \theta)}.$$

Thus, d_{crit} is the distance at which the second scan-
 261 ning plane intersects with the first scanning plane. For
 262 a particular scan point, the order with its predecessors
 263 should be reversed if its depth $d_{n,v}$ exceeds d_{crit} ; this
 264

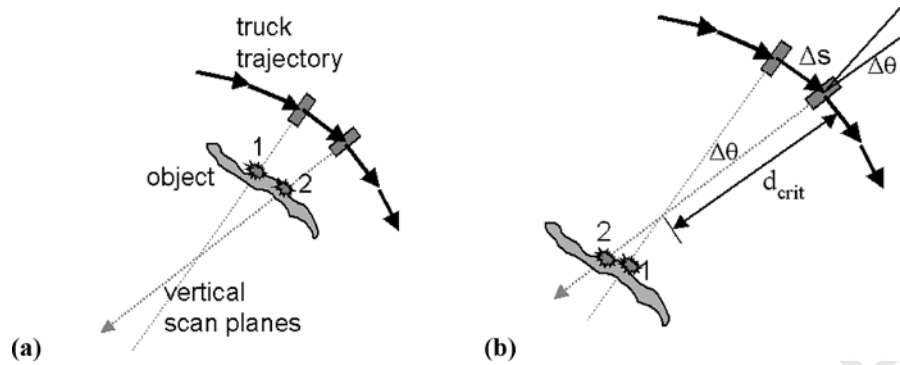


Figure 5. Scan geometry during a turn: (a) normal scan order for closer objects; (b) reversed scan order for farther objects.

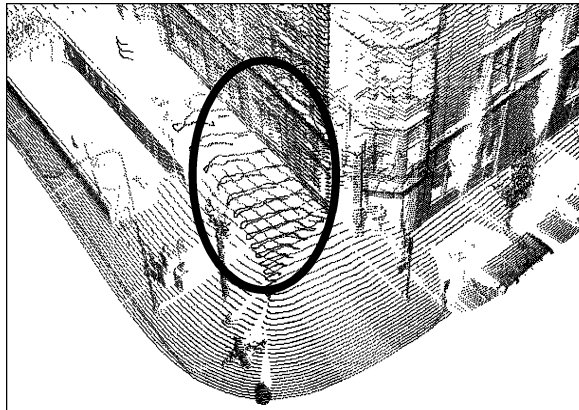


Figure 6. Scan points with reversed order.

265 means that its geometric location is somewhere in
 266 between points of previous scans. The effect of such order
 267 reversal can be seen in the marked area in Fig. 6. At the
 268 corner, the ground and the building walls are scanned
 269 twice, first from a direct view and then from an oblique
 270 angle, and hence with significantly lower accuracy. For
 271 the oblique points, the scans are out of order, destroy-
 272 ing the regular topology between neighboring scan
 273 points.

274 Since the “out of order” scans obtained in these sce-
 275 narios correspond to points that have already been cap-
 276 tured by “in order” scans, and are therefore redundant,
 277 our approach is to discard them and use only “in or-
 278 der” scans. For typical values of displacement, turn-
 279 ing angle, and distance of structures from our driving
 280 path, this occurs only in scans of turns with significant
 281 angular changes. By removing these “turn” scans and
 282 splitting the path at the “turning points”, we obtain path
 283 segments with low curvature that can be considered as
 284 locally quasi-linear, and can therefore be conveniently

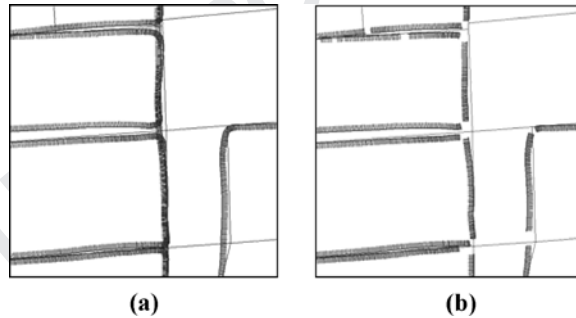


Figure 7. Driven path: (a) before segmentation; (b) after segmen-
 tation into quasi-linear segments.

285 processed as depth images, as described later in this
 286 section. In addition, to ensure that these segments are
 287 not too large for further processing, we subdivide them
 288 if they are larger than a certain size; specifically, in
 289 segments that are longer than 100 meters, we identify
 290 vertical scans that have the fewest scan points above
 291 street level, corresponding to gaps between buildings,
 292 and segment at these locations. Furthermore, we detect
 293 redundant path segments for areas captured multiple
 294 times due to multiple drive-bys, and use only one of
 295 them for reconstruction purposes. Figures 7(a) and (b)
 296 show an example of an original path, and the resulting
 297 path segments overlaid on a road map, respectively.
 298 The small lines perpendicular to the driving path indi-
 299 cate the scanning plane of the vertical scanner for each
 300 position.

3.2. Converting Path Segments into Depth Images 301

In the previous subsection, we described how to create
 path segments that are guaranteed to contain no scan

304 pairs with permuted horizontal order. As the vertical
 305 order is inherent to the scan itself, all scan points of a
 306 segment form a 3D scan grid with regular, quadrilateral
 307 topology. This 3D scan grid allows us to transform the
 308 scan points into a depth image, i.e. a 2.5D representa-
 309 tion where each pixel represents a scan point, and the
 310 gray value for each pixel is proportional to the depth
 311 of the scan point. The advantage of a depth image is its
 312 intuitively easy interpretation, and the increased pro-
 313 cessing speed the 2D domain provides. However, most
 314 operations that are performed on the depth image can
 315 be done just as well on the 3D point grid directly, only
 316 not as conveniently.

317 A depth image is typically used for representing data
 318 from 3D scanners. Even though the way the depth value
 319 is assigned to each pixel is dependent on the specific
 320 scanner, in most cases it is the distance between scan
 321 point and scanner origin, or its cosine with respect to
 322 the ground plane. As we expect mainly vertical struc-
 323 tures, we choose the latter option and use the depth
 324 $d_{n,v} = \cos(\nu) \cdot s_{n,v}$ rather than the distance $s_{n,v}$, so
 325 that the depth image is basically a tilted height field.
 326 The advantage is that in this case points that lie on a
 327 vertical line, e.g. a building wall, have the same depth
 328 value, and are hence easy to detect and group. Note
 329 that our depth image differs from one that would be
 330 obtained from a normal 3D scanner, as it does not have
 331 a single center from which the scan points are mea-
 332 sured; instead, there are different centers for each in-
 333 dividual vertical column along the path segment. The
 334 obtained depth image is neither a polar nor a parallel
 335 projection; it resembles most to a cylindrical projec-
 336 tion. Due to non-uniform driving speed and non-linear
 337 driving direction, these centers are in general not on a
 338 line, but on an arbitrary shaped, though low-curvature
 339 curve, and the spacing between them is not exactly uni-
 340 form. Because of this, strictly speaking the grid position
 341 only specifies the topological order of the depth pix-
 342 els, and not the exact 3D point coordinates. However,
 343 as topology and depth value are a good approximation
 344 for the exact 3D coordinates, especially within a small
 345 neighborhood, we choose to apply our data process-
 346 ing algorithms to the depth image, thereby facilitating
 347 use of standard image processing techniques such as
 348 region growing. Moreover, the actual 3D vertex coord-
 349 inates are still kept and used for 3D operations such as
 350 plane fitting. Figure 8(a) shows an example of the 3D
 351 vertices of a scan grid, and Fig. 8(b) shows its corre-
 352 sponding depth image, with a gray scale proportional to
 353 $d_{n,v}$.

4. Properties of City Laser Scans 354

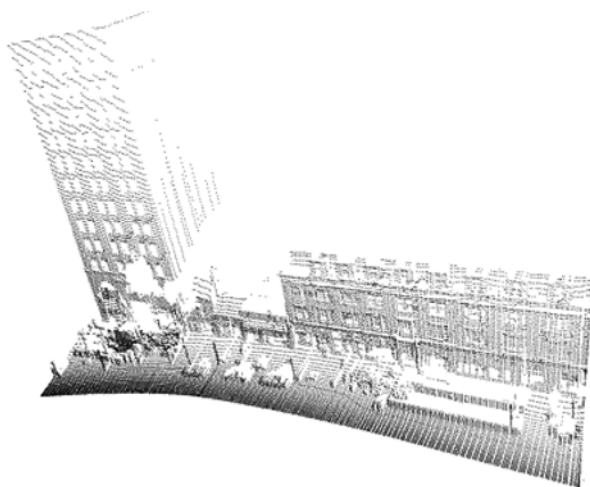
355 In this section, we briefly describe properties of scans
 356 taken in a city environment, resulting from the physics
 357 of a laser scanner as an active device measuring time-
 358 of-flight of light rays. It is essential to understand these
 359 properties and the resulting imperfections in distance
 360 measurement, since at times they lead to scan points
 361 that appear to be in contradiction with human eye per-
 362 ception or a camera. As the goal of our modeling ap-
 363 proach is to generate a photo realistic model, we are
 364 interested in reconstructing what the human eye or a
 365 camera would observe while moving around in the city.
 366 As such, we discuss the discrepancies between these
 367 two different sensing modalities in this section.

4.1. Discrepancies Due to Different Resolution 368

369 The beam divergence of the laser scanner is about 15
 370 milliradians (mrad) and the spacing, hence the angu-
 371 lar resolution, is about 17 mrad. As such, this is much
 372 lower than the resolution of the camera image with
 373 about 2.1 mrad in the center and 1.4 mrad at the image
 374 borders. Therefore, small or thin objects, such as ca-
 375 bles, fences, street signs, light posts and tree branches,
 376 are clearly visible in the camera image, but only par-
 377 tially captured in the scan. Hence they appear as “float-
 378 ing” vertices, as seen in the depth image in Fig. 9.

4.2. Discrepancies Due to the Measurement Physics 379

380 Camera and eye are passive sensors, capturing light
 381 from an external source; this is in contrast with a laser
 382 scanner, which is an active sensor, and uses light that
 383 it emits itself. This results in substantial differences
 384 in measurement of reflecting and semitransparent sur-
 385 faces, which are in form of windows and glass fronts
 386 frequently present in urban environments. Typically,
 387 there is at least 4% of the light reflected at a single
 388 glass/air transition, so a total of at least 8% per win-
 389 dow; if the window has a reflective coating, this can be
 390 larger. The camera typically sees a reflection of the sky
 391 or a nearby building on the window, often distorted or
 392 merged with objects behind the glass. Although most
 393 image processing algorithms would fail in this situa-
 394 tion, the human brain is quite capable of identifying
 395 windows. In contrast, depending on the window re-
 396 flectance, the laser beam is either entirely reflected,
 397 most times in a different direction from the laser itself,



(a)



(b)

Figure 8. Scan grid representations: (a) 3D vertices; (b) depth image.

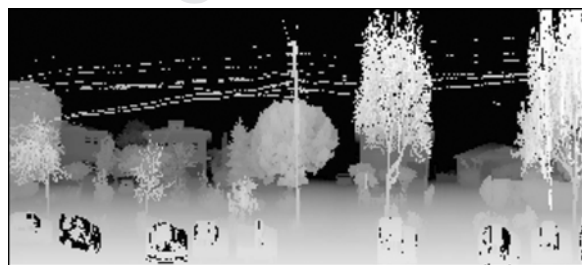


Figure 9. "Floating" vertices.

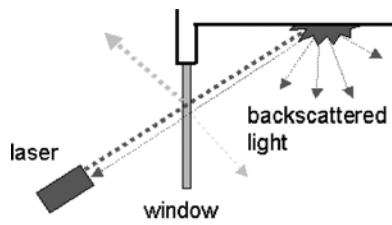


Figure 10. Laser measurement in case of a glass window.

398 resulting in no distance value, or is transmitted through
399 the glass. In the latter case, if it hits a surface as shown
400 in Fig. 10, the backscattered light travels again through
401 the glass. The resulting surface reflections on the glass
402 only weaken the laser beam intensity, eventually below

the detection limit, but do not otherwise necessarily af- 403
fect the distance measurement. To the laser, the window 404
is quasi non-existent, and the measurement point is gen- 405
erally not on the window surface, unless the surface is 406
orthogonal to the beam. In case of multi-reflections, the 407

408 situation becomes even worse as the measured distance
 409 is almost random.

410 4.3. *Discrepancies Due to Different Scan*
 411 *and Viewpoints*

412 Laser and camera are both limited in that they can only
 413 detect the first visible/backscattering object along a
 414 measurement direction and as such cannot deal with
 415 occlusions. If there is an object in the foreground, such
 416 as a tree in front of a building, the laser cannot cap-
 417 ture what is behind it; hence, generating a mesh from
 418 the obtained scan points results in a hole in the build-
 419 ing. We refer to this type of mesh hole as *occlusion*
 420 *hole*. As the laser scan points resemble a cylindrical
 421 projection, but rendering is parallel or perspective, in
 422 presence of occlusions, it is impossible to reconstruct
 423 the original view without any holes, even for the view-
 424 points from which data was acquired. This is a special
 425 property of our fast 2D data acquisition method. An
 426 interesting fact is that the wide-angle camera images
 427 captured simultaneously with the scans often contain
 428 parts of the background invisible to the laser. These
 429 could be potentially used either to fill in geometry using
 430 stereo techniques, or to verify the validity of the
 431 filled in geometry obtained from using interpolation
 432 techniques.

433 For a photo realistic model, we need to devise
 434 techniques for detecting discrepancies between the
 435 two modalities, removing invalid scan points, and
 436 filling in holes, either due to occlusion or due to
 437 unpredictable surface properties; we will describe
 438 our approaches to these problems in the following
 439 sections.

440 5. **Multi-Layer Representation**

441 To ensure that the facade model looks reasonable from
 442 every viewpoint, it is necessary to complete the geom-
 443 etry for the building facades. Typically, our facades are
 444 2 1/2 D objects rather than full 3D objects, and hence
 445 we introduce a representation based of multiple depth
 446 layers for the street scenery, similar to the one pro-
 447 posed in Chang and Zakhor (1999). Each depth layer
 448 is a scan grid, and the scan points of the original grid
 449 are assigned to exactly one of the layers. If at a certain
 450 grid location there is a point in a foreground layer, this
 451 location is empty in all layers behind it and needs to be
 452 filled in.

453 Even though the concept can be applied to an arbitrary
 454 number of layers, we found that it is in our case
 455 sufficient to generate only two, namely a foreground
 456 and a background layer. To assign a scan point to ei-
 457 ther one of the two layers we make the following ass-
 458 sumptions about our environment: Main structures, i.e.
 459 buildings, are usually (a) vertical, and (b) extend over
 460 several feet in horizontal dimension. Furthermore, we
 461 assume that (c) building facades are roughly perpen-
 462 dicular to the driving direction and that (d) most scan
 463 points correspond to facades rather than to foreground
 464 objects, as it can occur in residential areas with houses
 465 hidden behind trees. Under these conditions, we can ap-
 466 ply the following steps to identify foreground objects:

467 For each vertical scan n corresponding to a column in
 468 the depth image, we define the main depth as the depth
 469 value that occurs most frequently, as shown in Fig. 11.
 470 The scan vertices corresponding to the main depth lie
 471 on a vertical line, and the first assumption suggests that
 472 this is a main structure, such as a building, or perhaps
 473 other vertical objects, such as a street light or a tree
 474 trunk. With the second assumption, we filter out the
 475

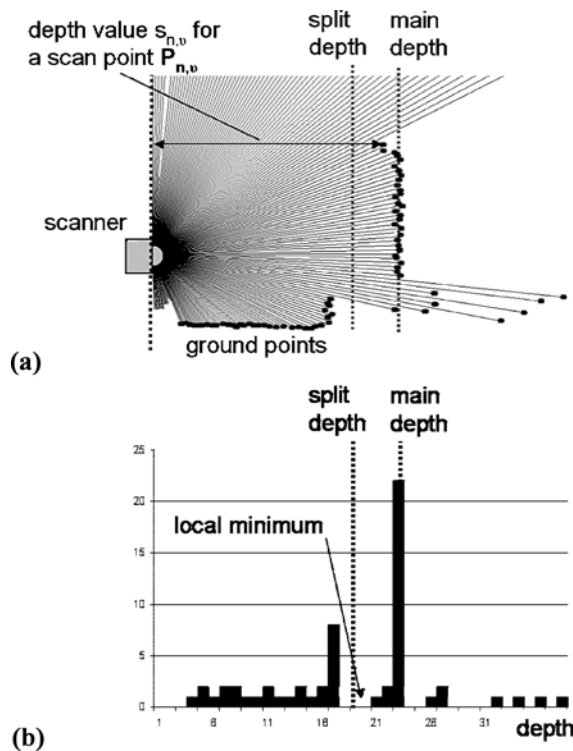


Figure 11. Main depth computation for a single scan n : (a) laser scan with rays indicating the laser beams and dots at the end of the corresponding scan points; (b) computed depth histogram.

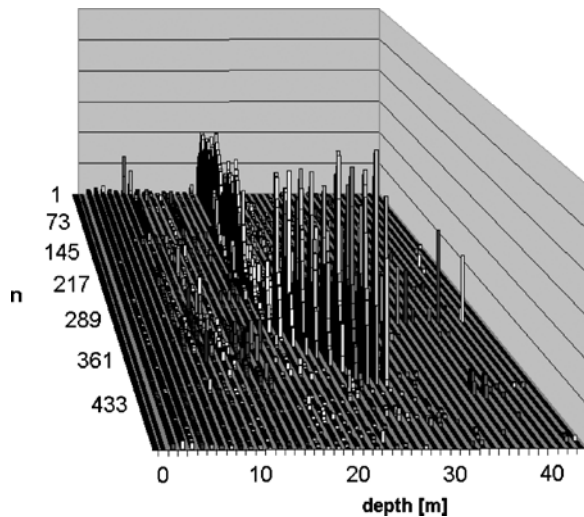


Figure 12. Two-dimensional histogram for all scans.

475 latter class of vertical objects. More specifically, our
476 processing steps can be described as follows:

477 We sort all depth values $s_{n,v}$ for each column n of
478 the depth image into a histogram as shown in Fig. 11(a)
479 and (b), and detect the peak value and its correspond-
480 ing depth. Applying this to all scans results in a 2D
481 histogram as shown in Fig. 12, and an individual main

depth value estimate for each scan. Based on the second
482 assumption, isolated outliers are removed by applying
483 a median filter on these main depth values across the
484 scans, and a final depth value is assigned to each col-
485 umn n . We define a “split” depth, γ_n , for each column
486 n , and set it to the first local minimum of the histogram
487 occurring immediately before main depth, i.e. with a
488 depth value smaller than the main depth. Taking the first
489 minimum in the distribution instead of the main value
490 itself has the advantage that points clearly belonging
491 to foreground layers are splits off, whereas overhang-
492 ing parts of buildings, for which the depth is slightly
493 smaller than the main depth, are kept in the main layer
494 where they logically belong to, as shown in Fig. 11. 495

A point can be identified as a ground point if its z co-
496 ordinate has a small value and its neighbors in the same
497 scan column have a similarly low z value. We prefer
498 to include the ground in our models, and as such, as-
499 sign ground points also to the background layer. There-
500 fore, we split layers by assigning a scan point $P_{n,v}$ to
501 the background layer, if $s_{n,v} > \gamma_n$ or $P_{n,v}$ is a ground
502 point, and to the foreground layer otherwise. Figure 13
503 shows an example for the resulting foreground and
504 background layers. 505

506 Since the steps described in this section assume the
presence of vertical buildings, they cannot be expected



Figure 13. (a) Foreground layer; (b) background layer.

507 to work for segments that are dominated by trees; this
 508 also applies to the processing steps we introduce in
 509 the following sections. As our goal is to reconstruct
 510 buildings, path segments can be left unprocessed and
 511 included “as is” in the city model, if they do not contain
 512 any structure. A characteristic of a tree area is its fractal-
 513 like geometry, resulting in a large variance among ad-
 514 jacent depth values, or even more characteristically,
 515 many significant vector direction changes for the edges
 516 between connected mesh vertices. We define a coeffi-
 517 cient for the fractal nature of a segment by counting
 518 vertices with direction changes greater than a specific
 519 angle, e.g. twenty degrees, and dividing them by the
 520 total number of vertices. If this coefficient is large, the
 521 segment is most likely a tree area and should not be
 522 made subject to the processing steps described in this
 523 section. This is for example the case for the segment
 524 shown in Fig. 9.

525 After splitting layers, all grid locations occupied in
 526 the foreground layer are missing in the background
 527 layer as the vertical laser does not capture any oc-
 528 cluded geometry; in the next section we will describe
 529 an approach for filling these missing grid locations
 530 based on neighboring pixels. However, in our data ac-
 531 quisition system there are 3D vertices available from
 532 other sources, such as stereo vision and the horizon-
 533 tal scanner used for navigation. Thus, it is conceiv-
 534 able to use this additional information to fill some
 535 in the depth layers. Our approach to doing so is as
 536 follows:

537 Given a set of 3D vertices V_i obtained from a dif-
 538 ferent modality, determine the closest scan direction
 539 for each vertex and hence the grid location (n, v) it
 540 should be assigned to. As shown in Fig. 14, each V_i
 541 is assigned to the vertical scanning plane, S_n , with the
 542 smallest Euclidean distance, corresponding to column

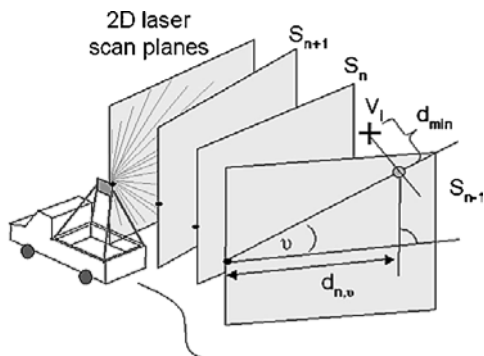


Figure 14. Sorting additional points into the layers.



Figure 15. Background layer after sorting in additional points from other modalities.

n in the depth image. Using simple trigonometry, the
 scanning angle under which this vertex appears in the
 scanning plane, and hence the depth image row v , can
 be computed, as well as the depth $d_{n,v}$ of the pixel.

We can now use these additional vertices to fill in
 the holes. To begin with, all vertices that do not belong
 to background holes are discarded. If there is exactly
 one vertex falling onto a grid location, its depth is di-
 rectly assigned to that grid location; for situations with
 multiple vertices, median depth value for this location
 is chosen. Figure 15 shows the background layer from
 Fig. 13(b) after sorting in 3D vertices from stereo vi-
 sion and horizontal laser scans. As seen, some holes
 can be entirely filled in, and the size of others becomes
 smaller, e.g. the holes due to trees in the tall building on
 the left side. Note that this intermediate step is optional
 and depends on the availability of additional 3D data.

6. Background Layer Postprocessing and Mesh Generation

In this section, we will describe a strategy to remove
 erroneous scan points, and to fill in holes in the back-
 ground layer. There exists a variety of successful hole
 filling approaches, for example based on fusing mul-
 tiple scans taken from different positions (Curless and
 Levoy, 1996; Stamos and Allen, 2002). Most previ-
 ous work on hole filling in the literature has been fo-
 cused on reverse engineering applications, in which a
 3D model of an object is obtained from multiple laser
 scans taken from different locations and orientations.
 Since these existing hole filling approaches are not ap-
 plicable to our experimental setup, our approach is to
 estimate the actual geometry based on the surrounding
 environment and reasonable heuristics. One cannot ex-
 pect this estimate to be accurate in *all* possible cases,
 rather to lead to an acceptable result in *most* cases, thus

578 reducing the amount of further manual interventions
 579 and postprocessing drastically. Additionally, the esti-
 580 mated geometry could be made subject to further veri-
 581 fication steps, such as consistency checks by applying
 582 stereo vision techniques to the intensity images cap-
 583 tured by the camera.

584 Our data typically exhibits the following character-
 585 istics:

- 586 • Occlusion holes, such as those caused by a tree,
 587 are large and can extend over substantial parts of a
 588 building.
- 589 • A significant number of scan points surrounding a
 590 hole may be erroneous due to glass surfaces.
- 591 • In general, a spline surface filling is unsuitable, as
 592 building structures are usually piecewise planar with
 593 sharp discontinuities.
- 594 • The size of data set resulting from a city scan is huge,
 595 and therefore the processing time per hole should be
 596 kept to a minimum.

597 Based on the above observations, we propose the
 598 following steps for data completion.

599 6.1. *Detecting and Removing Erroneous Scan* 600 *Points in the Background layer*

601 We assume that erroneous scan points are due to
 602 glass surfaces, i.e. the laser measured either an in-
 603 ternal wall/object, or a completely random distance
 604 due to multi-reflections. Either way, the depth of the
 605 scan points measured through the glass is substantially
 606 greater than the depth of the building wall, and hence
 607 these points are candidates for removal. Since glass
 608 windows are usually framed by the wall, we remove
 609 the candidate points only if they are embedded among
 610 a number of scan points at main depth. An example
 611 of the effect of this step can be seen by comparing the
 612 windows of the original image in Fig. 16(a) with the
 613 processed background layer in Fig. 16(b).

614 6.2. *Segmenting the Occluding Foreground Layer* 615 *into Objects*

616 In order to determine holes in the background layer
 617 caused by occlusion, we segment the occluding fore-
 618 ground layer into objects and project segmentation onto
 619 the background layer. This way, holes can be filled in
 620 one “object” at a time, rather than all at the same time;
 621 this approach has the advantage that more localized



(a)



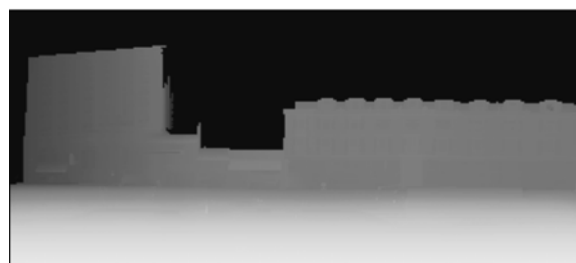
(b)



(c)



(d)



(e)

Figure 16. Processing steps of depth image. (a) Initial depth image. (b) Background layer after removing invalid scan points. (c) Foreground layer segmented. (d) Occlusion holes filled. (e) Final background layer after filling remaining holes.

622 hole filling algorithms are more likely to result in vi-
 623 sually pleasing models than global ones. We segment
 624 the foreground layer by taking a random seed point
 625 that does not yet belong to a region, and applying a
 626 region growing algorithm that iteratively adds neigh-
 627 boring pixels if their depth discontinuity or their local
 628 curvature is small enough. This is repeated until all pix-
 629 els are assigned to a region, and the result is a region
 630 map as shown in Fig. 16(c). For each foreground re-
 631 gion, we determine boundary points on the background
 632 layer; these are all the valid pixels in the background
 633 layer that are close to hole pixels caused by the occlud-
 634 ing object.

635 6.3. Filling Occlusion Holes in the Background 636 Layer for Each Region

637 As the foreground objects are located in front of main
 638 structures and in most cases stand on the ground, they
 639 occlude not only parts of a building, but also parts of
 640 the ground. Specifically, an occlusion hole caused by
 641 a low object, such as a car, with a large distance to
 642 the main structure behind it, is typically located only
 643 in the ground and not in the main structure. This is be-
 644 cause the laser scanner is mounted on top of a rack, and
 645 as such has a top down view of the car. As a plane is a
 646 good approximation to the ground, we fill in the ground
 647 section of an occlusion hole by the ground plane. There-
 648 fore, for each depth image column, i.e. each scan, we
 649 compute the intersection point between the line through
 650 the main depth scan points and the line through ground
 651 scan points. The angle ν'_n at which this point appears
 652 in the scan marks the virtual boundary between ground
 653 part and structure part of the scan; we fill in structure
 654 points above and ground points below this boundary
 655 differently.

656 Applying a RANSAC algorithm, we find the plane
 657 with the maximum consensus, i.e. maximum number
 658 of ground boundary points on it, as the optimal ground
 659 plane for that local neighborhood. Each hole pixel with
 660 $\nu < \nu'_n$ is then filled in with a depth value according
 661 to this plane. It is possible to apply the same techni-
 662 que for the structure hole pixels, i.e. the pixels with
 663 $\nu > \nu'_n$, by finding the optimal plane through the struc-
 664 ture boundary points and filling in the hole pixels ac-
 665 cordingly. However, we have found that in contrast to
 666 the ground, surrounding building pixels do not often
 667 lie on a plane. Instead, there are discontinuities due to
 668 occluded boundaries and building features such as mar-
 669 quees or lintels, in most cases extending horizontally

across the building. Therefore, rather than filling holes
 with a plane, we fill in structure holes line by line hori-
 zontally, in such a way that the depth value at each pixel
 is the linear interpolation between the closest right and
 left structure boundary point, if they both exist; other-
 wise no value is filled in. In a second phase, a similar
 interpolation is done vertically, using the already filled
 in points as valid boundary points. This method is not
 only simple and therefore computationally efficient, it
 also takes into account the surrounding horizontal fea-
 tures of the building in the interpolation. The resulting
 background layer is shown in Fig. 16(d).

6.4. Postprocessing the Background Layer

The resulting depth image and the corresponding 3D
 vertices can be improved by removing scan points that
 remain isolated, and by filling small holes surrounded
 by geometry using linear interpolation between neigh-
 boring depth pixels. The final background layer after
 applying all processing steps is shown in Fig. 16(e).

In order to create a mesh, each depth pixel can be
 transformed back into a 3D vertex, and each vertex $P_{n,v}$
 is connected to a depth image neighbor $P_{n+\Delta n, v+\Delta v}$ if

$$|s_{n+\Delta n, v+\Delta v} - s_{n,v}| < s_{\max} \quad \text{or if} \\ \cos \varphi > \cos \varphi_{\max}$$

with

$$\cos \varphi = \frac{(\vec{P}_{n-\Delta n, v-\Delta v} - \vec{P}_{n,v}) \cdot (\vec{P}_{n,v} - \vec{P}_{n+\Delta n, v+\Delta v})}{|\vec{P}_{n-\Delta n, v-\Delta v} - \vec{P}_{n,v}| \cdot |\vec{P}_{n,v} - \vec{P}_{n+\Delta n, v+\Delta v}|}$$

Intuitively, neighbors are connected if their depth
 difference does not exceed a threshold s_{\max} or the
 local angle between neighboring points is smaller
 than threshold angle φ_{\max} . The second criteria is
 intended to connect neighboring points that are on a
 line, even if their depth difference exceeds s_{\max} . The
 resulting quadrilateral mesh is split into triangles, and
 mesh simplification tools such as Qslim (Garland and
 Heckbert, 1997) can be applied to reduce the number of
 triangles.

7. Atlas Generation for Texture Mapping

As photorealism cannot be achieved by using geometry
 alone, we need to enhance our model with texture data.
 To achieve this, we equip our data acquisition system
 with a digital color camera with a wide-angle lens. The

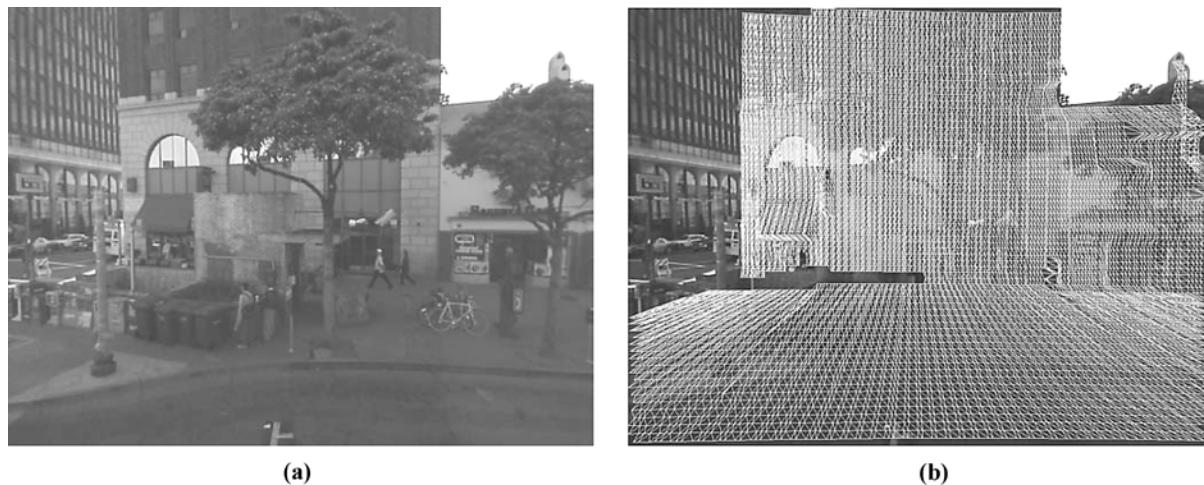


Figure 17. Background mesh triangles projected onto camera images. (a) Camera image. (b) Hole filled background mesh projected onto the image and shown as white triangles; occluded background triangles project onto foreground objects. The texture of foreground objects such as the trees should not be used for texturing background triangles corresponding to the building facade.

708 camera is synchronized with the two laser scanners,
 709 and is calibrated against the laser scanners' coordinate
 710 system; hence, the camera position can be computed for
 711 all images. After calibrating the camera and removing
 712 lens distortion in the images, each 3D vertex can be
 713 mapped to its corresponding pixel in an intensity image
 714 by a simple projective transformation. As the 3D mesh
 715 triangles are small compared to their distance to the
 716 camera, perspective distortions within a triangle can
 717 be neglected, and each mesh triangle can be mapped
 718 to a triangle in the picture by applying the projective
 719 transformation to its vertices.

720 As described in Section 4, camera and laser scanners
 721 have different viewpoints during data acquisition, and
 722 in most camera pictures, at least some mesh triangles
 723 of the background layer are occluded by foreground
 724 objects; this is particularly true for triangles that con-
 725 sist of filled-in points. An example of this is shown in
 726 Fig. 17 where occluded background triangles project
 727 onto foreground objects such as the tree. The back-
 728 ground triangles are marked in white in Fig. 17. Al-
 729 though the pixel location of the projected background
 730 triangles is correct, some of the corresponding texture
 731 triangles merely correspond to the foreground objects,
 732 and thus should not be used for texture mapping the
 733 background triangles.

734 In this section, we address the problem of segment-
 735 ing out the foreground regions in the images so that their
 736 texture is not used for the background mesh triangles.
 737 After segmentation, multiple images are combined into

a single texture atlas; we then propose a number of tech- 738
 niques to fill in the texture holes in the atlas resulting 739
 from foreground occlusion. The resulting hole filled at- 740
 las is finally used for texture mapping the background 741
 mesh. 742

7.1. Foreground/Background Segmentation 743 in the Images 744

A simple way of segmenting out the foreground objects 745
 is to project the foreground mesh onto the camera im- 746
 ages and mark out the projected triangles and vertices. 747
 While this process works adequately in most cases, it 748
 could miss out some parts of the foreground objects 749
 such as those shown in Fig. 18, where projected fore- 750
 ground geometry is marked in white. As seen in the 751
 figure, some small portions of the foreground tree are 752
 incorrectly considered as background. This is due to 753
 following reasons: 754

1. The foreground scan points are not dense enough 755
 for segmenting the image with pixel accuracy, es- 756
 pecially at the boundaries of foreground objects. 757
2. The camera captures side views of foreground 758
 objects whereas the laser scanner captures a direct 759
 view, as illustrated in Fig. 19. Hence, some 760
 foreground geometry does not appear in the 761
 laser scans and as such cannot be marked as 762
 foreground. 763

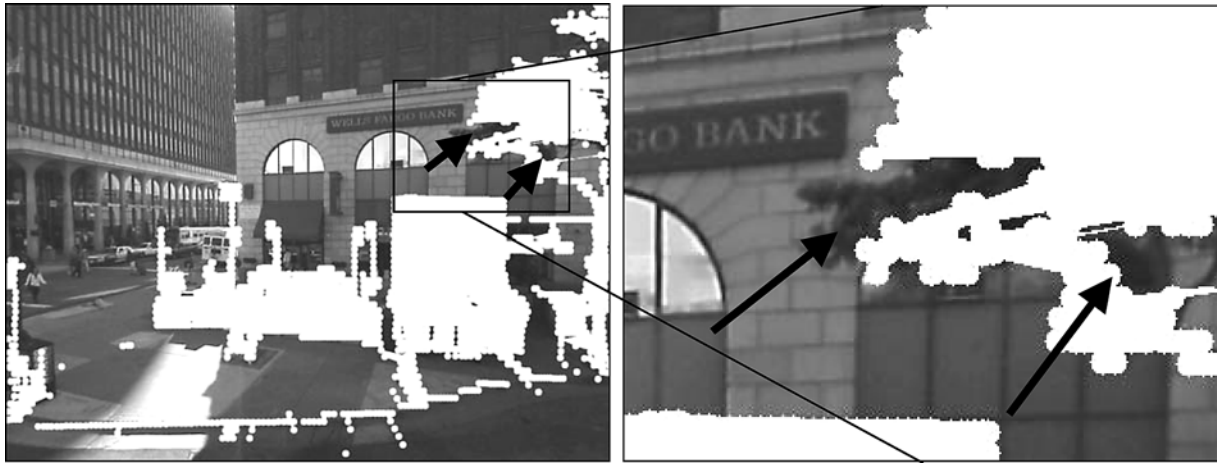


Figure 18. Identifying foreground in images by projection of the foreground mesh. White denotes the projected foreground and thus image areas not to be used for texture mapping of facades.

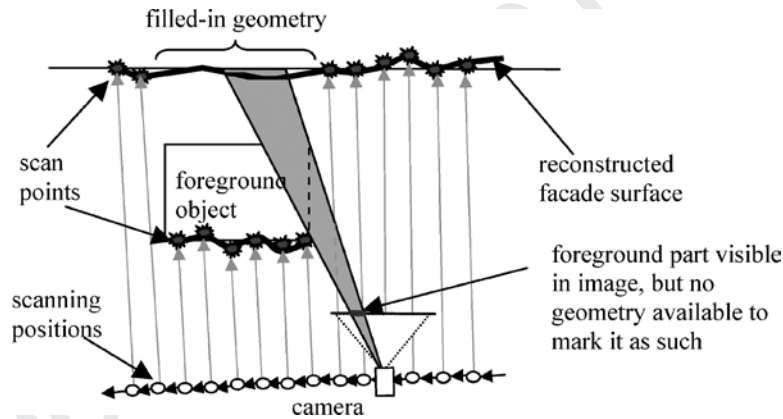


Figure 19. Some foreground objects at oblique viewing angle are not entirely marked in camera images.

764 To overcome this problem, we have developed a
765 second, more sophisticated method for pixel-accurate
766 foreground segmentation based on the use of corre-
767 spondence error. The overview of our approach is as
768 follows:
769 After splitting the scan points into the foreground
770 and background layers, the foreground scan points are
771 projected onto the images. A flood-filling algorithm is
772 applied to all the pixels within a window centered at
773 each of the projected foreground pixels using cues of
774 color constancy and correspondence error. The color
775 at every pixel in the window is compared to that of
776 the center pixel. If the colors are in agreement, and the
777 correspondence error value at the test pixel is close or
778 higher than the value at the center pixel, the test pixel
779 is assigned to the foreground.

In what follows we describe the notion of correspon- 780
dence error in more detail. Let $I = \{I_1, I_2, \dots, I_n\}$ 781
denote the set of camera images available for a quasi- 782
linear path segment. Consider two consecutive images 783
 I_{c-1} and I_c . Consider a 3D point \mathbf{x} belonging to the 784
background mesh obtained after geometry hole filling 785
described in Section 7. \mathbf{x} is projected to the images I_{c-1} 786
and I_c using the available camera position. Assuming 787
that the projected point is within the clip region of both 788
images, let its coordinates in I_{c-1} and I_c be denoted 789
by u_{c-1} and u_c respectively. If \mathbf{x} is not occluded by 790
any foreground object in an image, then its pixel co- 791
ordinates in the image belong to the background and 792
represent \mathbf{x} ; otherwise its pixel coordinates correspond 793
to the occluding foreground object. This leads to three 794
cases described below, and illustrated in Fig. 20: 795

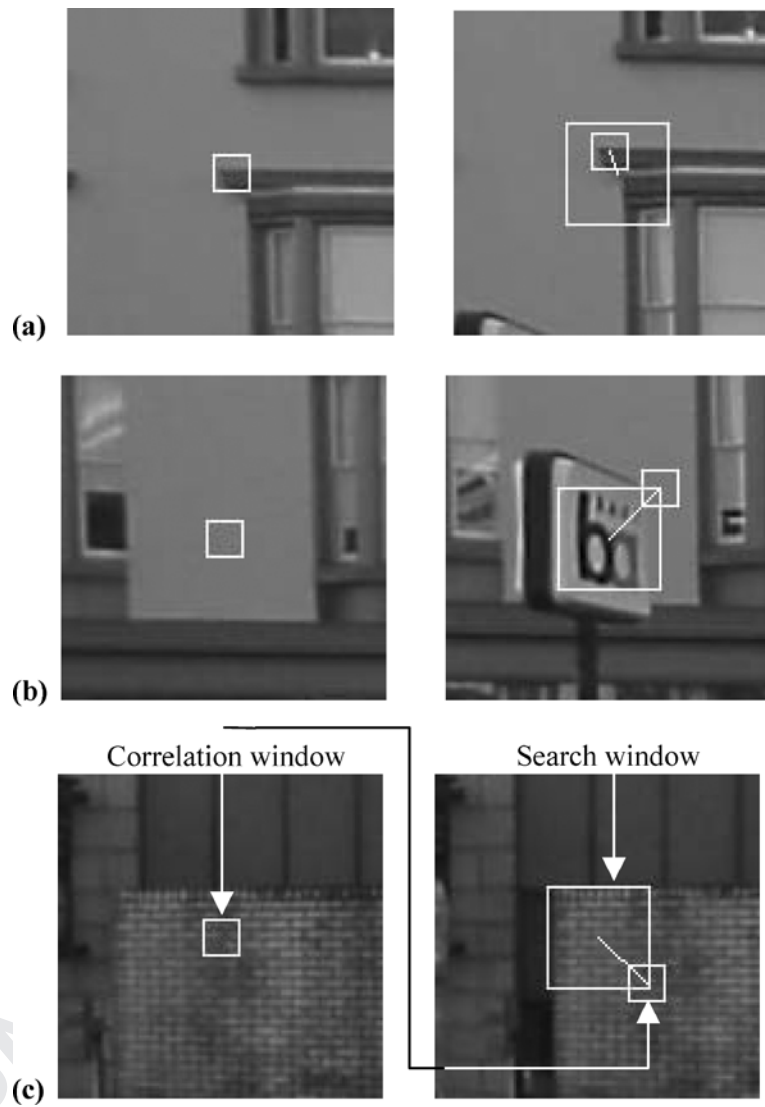


Figure 20. Illustration of correspondence error. (a) background scan point is unoccluded in both images. (b) background scan point occluded in one of the images. (c) background scan point occluded in both images. The search window and correlation window are marked for clarity. The line represents the correspondence error vector. The correlation window slides in the search window in order to find the best matching window.

- 796 1. x is occluded in neither images as shown in
797 Fig. 20(a); u_{c-1} , and u_c both belong to the back-
798 ground. If the camera position is known precisely,
799 u_c would be the correspondence point for u_{c-1} . In
800 practice, the camera position is known only approx-
801 imately, and taking u_{c-1} as a reference, its corre-
802 spondence point in I_c can be located close to u_c .
- 803 2. x is occluded only in one of the images as shown in
804 Fig. 20(b); one of u_{c-1} or u_c belongs to a foreground
805 object due to occlusion of point x , and the other
806 belongs to the background.

3. Point x is occluded in both images as shown in 807
808 Fig. 20(c), and both u_{c-1} and u_c belong to fore-
809 ground objects.

In all three cases the best matching pixel to u_{c-1} 810
811 in I_c , denoted by $u_{c-1,c}$, is found by searching in a
812 window centered around u_c , and performing color cor-
813 relation as illustrated in Fig. 20. The length of vec-
814 tor $\mathbf{v}(u_c, u_{c-1,c})$ then denotes the correspondence error
815 between u_{c-1} and u_c . If $|\mathbf{v}(u_c, u_{c-1,c})|$ is large, one
or both of u_{c-1} and u_c belong to a foreground object

816 resulting in cases 2 or 3. In the next step when im- 834
 817 ages I_c and I_{c+1} are considered, $\mathbf{v}(u_{c+1}, u_{c,c+1})$ is com- 835
 818 puted and we define the correspondence error at pixel 836
 819 u_c as:

$$\varepsilon(u_c) = \max(|\mathbf{v}(u_c, u_{c-1,c})|, |\mathbf{v}(u_{c+1}, u_{c,c+1})|)$$

820 Intuitively, if the correspondence error at a pixel is large 837
 821 the pixel likely belongs to a foreground object. The 838
 822 above equation is used to compute the correspondence 839
 823 error at all the pixels corresponding to projected back- 840
 824 ground scan points. To compute the correspondence 841
 825 error at all other pixels within the window centered at 842
 826 each of the projected foreground scan points, we apply 843
 827 nearest neighbor interpolation. Each pixel in the win- 844
 828 dow is declared to be foreground if (a) its color is in 845
 829 agreement with the center pixel, and (b) its correspon- 846
 830 dence error value is close or higher than the value at 847
 831 the center pixel.

832 The max operation in the above equation has the ef- 848
 833 fect of not missing out any foreground pixels. Even 849
 though this approach results in large values of cor-

834
 835
 836
 837
 838
 839
 840
 841
 842
 843
 844

1. The flood filling algorithm is applied to projected foreground scan points only within a square window w , the size of which is 61×61 pixels in our case; so if a background pixel has a high value of ε but has no projected foreground scan point within a neighborhood equal to size of w , it is never subjected to flood filling and thus never marked as foreground. 845
846
847
848
849
850
851
852
853
2. Marking non-foreground pixels as foreground is not as problematic as leaving foreground pixels unmarked. This is because the same 3D point is observed in multiple camera images, and even though it may be incorrectly classified as foreground in some images, it is likely to be correctly classified as background in others. On the other hand incorrect assignment of foreground pixels to the background and using then for texturing, results in a erroneous texture as discussed before. 845
846
847
848
849
850
851
852
853

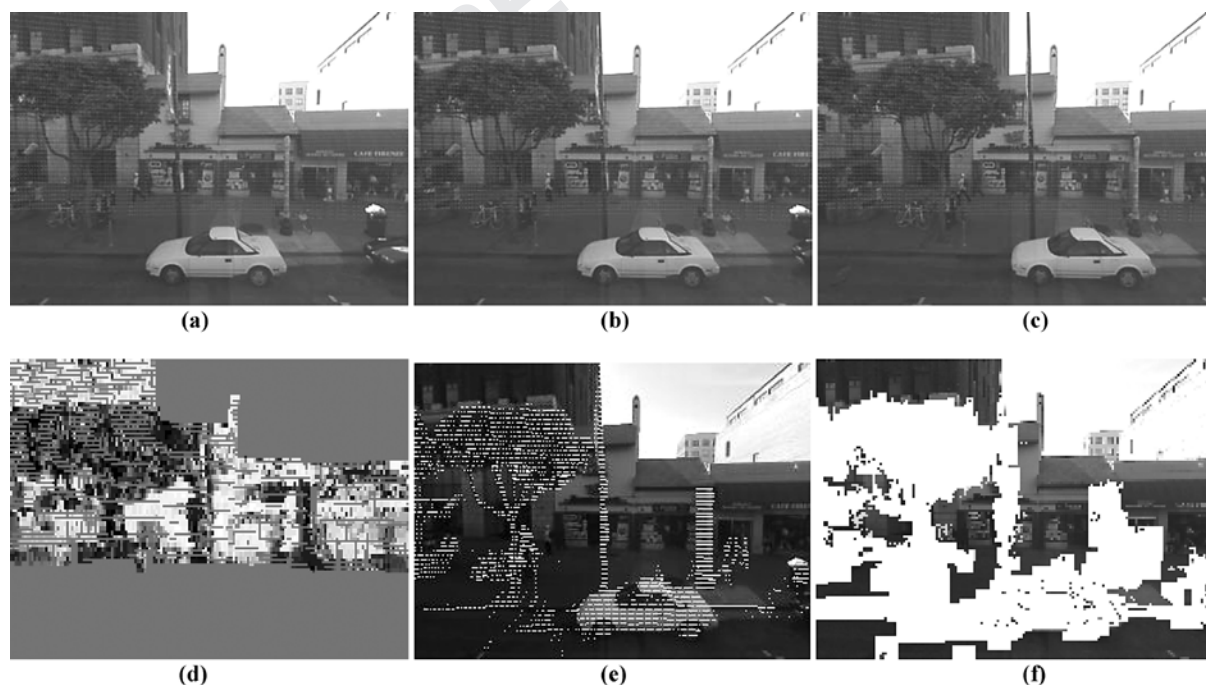


Figure 21. (a), (b), (c) sequence of three camera images I_{c-1} , I_c , I_{c+1} . (d) correspondence error for I_c shown as gray values. White corresponds to low value and black corresponds to high value of ε . Red pixels are pixels where no background scan points projected. ε is not computed at these pixels. (e) Foreground scan points marked as white pixels. (f) Foreground regions of I_c marked as white, using color constancy and correspondence error. The green triangles are the triangles used for texture mapping/atlas generation from this image.

Data Processing Algorithms for Generating Textured 3D Building Facade Meshes 175

854 Figures 21(a)–(c) show a sequence of three camera
 855 images, and Fig. 21(d) shows the correspondence
 856 error for the center image shown as gray values; the
 857 gray values have been scaled so that 0 or black corre-
 858 sponds to maximum value of ϵ , and 255 or white cor-
 859 responds to minimum value of ϵ . The correspondence
 860 error has been computed for each projected background
 861 scan point. A 7×7 window is centered at each pro-
 862 jected background scan point, and ϵ at all pixels in the
 863 window has been determined using nearest neighbor
 864 interpolation. The red pixels denote those for which
 865 ϵ has not been computed or interpolated in the im-
 866 age. The image looks like a roughly segmented fore-
 867 ground and background. Figure 21(e) shows the pro-
 868 jected foreground scan points marked as white pixels.¹
 869 Figure 21(f) shows the foreground segmentation using
 870 flood-filling with color and correspondence error com-
 871 parisons as explained in this section. The foreground
 872 has been marked in white color. The green triangles
 873 are the triangles used for texture mapping/atlas gener-
 874 ation from this image. As seen, there are some back-
 875 ground pixels that have been incorrectly assigned to the
 876 foreground. This can be attributed to the fact that our
 877 algorithm has been purposely biased to maximize the
 878 size of foreground region in order to avoid erroneously
 879 assigning background pixels to foreground.

880 7.2. *Texture Atlas Generation*

881 Since most parts of a camera image correspond to ei-
 882 ther foreground objects, or facade areas visible in other
 883 images at a more direct view, we can reduce the amount
 884 of texture imagery by extracting only the parts actually
 885 used. The vertical laser scanner results in a vertical col-
 886 umn of scan points, and triangulation of the scan points
 887 thus results in a mesh with a row-column structure as
 888 can be seen in Fig. 17(b). The inherent row-column
 889 structure of the triangular mesh permits to assemble a
 890 new artificial image with a corresponding row-column
 891 structure, and reserved spaces for each texture triangle.
 892 This so-called *texture atlas* is created by performing
 893 the following steps: (a) Determining the inter-column
 894 and inter-row spacing for each consecutive column and
 895 row pair in the mesh and using this to reserve space in
 896 the atlas. (b) Warping each texture triangle to fit to the
 897 corresponding reserved space in the atlas and copying
 898 it into the atlas. (c) Setting texture coordinates of the
 899 mesh triangles to the location in the atlas.

900 Since in this manner the mesh topology of the tri-
 901 angles is preserved and adjacent triangles align auto-

902 matically due to the warping process, the resulting tex-
 903 ture atlas resembles a mosaic image. While the atlas
 904 image might not visually look precisely proportionate
 905 due to slightly non-uniform spacing between vertical
 906 scans, these distortions are inverted by the graphics
 907 card hardware during the rendering process, and are
 908 thus negligible.

909 Figures 22(a) and (b) illustrate the atlas generation:
 910 From the acquired stream of images, the utilized texture
 911 triangles are copied into the texture atlas as symbolized
 912 by the arrows. In this illustration, only five original im-
 913 ages are shown; in this example we have actually com-
 914 bined 58 images of 1024×768 pixels size to create
 915 a texture atlas of 3180×540 pixels. Thus, the texture
 916 size is reduced from 45.6 million pixels to 1.7 mil-
 917 lion pixels, while the resolution remains the same. If
 918 occluding foreground objects and building facade are
 919 too close, some facade triangles might not be visible
 920 in any of the captured imagery, and hence cannot be
 921 texture mapped at all. This leaves visually unpleasant
 922 *holes* in the texture atlas, and hence in final rendering
 923 of the 3D models. In the following, we propose ways of
 924 synthesizing plausible artificial texture for these holes.

7.3. *Hole Filling of the Atlas*

925 Early work relating to disocclusion in images was done
 926 by Nitzberg et al. (1993). Significant improvements
 927 to this were made in Masnou and Morel (1998) and
 928 Ballester et al. (2000, 2001). These methods are capable
 929 of filling in small holes in non-textured regions and
 930 essentially deal with *local Inpainting*; they thus cannot
 931 be used for filling in large holes or holes in textured
 932 regions (Chan and Shen, 2001). We propose a simple
 933 and efficient method of hole filling that first completes
 934 regions of low spatial frequency by interpolating the
 935 values of surrounding pixels, and then uses a copy-paste
 936 method to synthesize artificial texture for the holes.
 937 In what follows, we explain the above steps in more
 938 detail.

940 **Horizontal and Vertical Interpolation.** Our pro-
 941 posed algorithm first fills in holes in regions of low
 942 variance using linear interpolation of surrounding pixel
 943 values. A generalized two-dimensional (2D) linear in-
 944 terpolation is not advantageous over a one-dimensional
 945 (1D) interpolation in a man-made environment where
 946 features are usually either horizontal or vertical e.g.
 947 curbs run across the streets horizontally, edges of fa-
 948 cades are vertical, banners on buildings are horizontal.



Figure 22. (a) Images obtained after foreground segmentation are combined to create a texture atlas. In this illustration only five images were shown, whereas in this particular example 58 images were combined to create the texture atlas. (b) Atlas with texture holes for the facade portions that were not visible in any image. (c) Artificial texture is synthesized in the texture holes to result in a filled in atlas that is finally used for texturing the background mesh.

949 One-dimensional interpolation is simple, and is able to
 950 recover most sharp discontinuities and gradients. We
 951 perform 1D horizontal interpolation in the following
 952 way: for each row, pairs of pixels between which RGB
 953 information is missing are detected. The missing values
 954 are filled in by a linear interpolation of the boundary
 955 pixels if (a) the boundary pixels at the two ends have
 956 similar values, and (b) the variances around the bound-
 957 aries are low at both ends. We follow this by vertical
 958 interpolation in which for each column the missing val-
 959 ues are interpolated vertically.

960 Figure 23(a) shows part of a texture atlas with holes
 961 marked in red. Figure 23(b) shows the image after a
 962 pass of 1D horizontal interpolation. As seen, horizontal

edges such as the blue curb are completed. Figure 23(c) 963
 shows the image after horizontal and vertical interpo- 964
 lation. We find the interpolation process to be simple, 965
 fast, and to complete the low frequency regions well. 966

The Copy-Paste Method. Assuming that building facade 967
 are highly repetitive, we fill holes that could not 968
 be filled by horizontal and vertical interpolation, by 969
 copying and pasting blocks from other parts of the im- 970
 age. This approach is similar to the one proposed in 971
 Efros and Freeman (2001) where a large image is cre- 972
 ated with a texture similar to a given template. In our 973
 copy-paste method the image is scanned pixel by pixel 974
 in raster scan order, and pixels at the boundary of holes 975

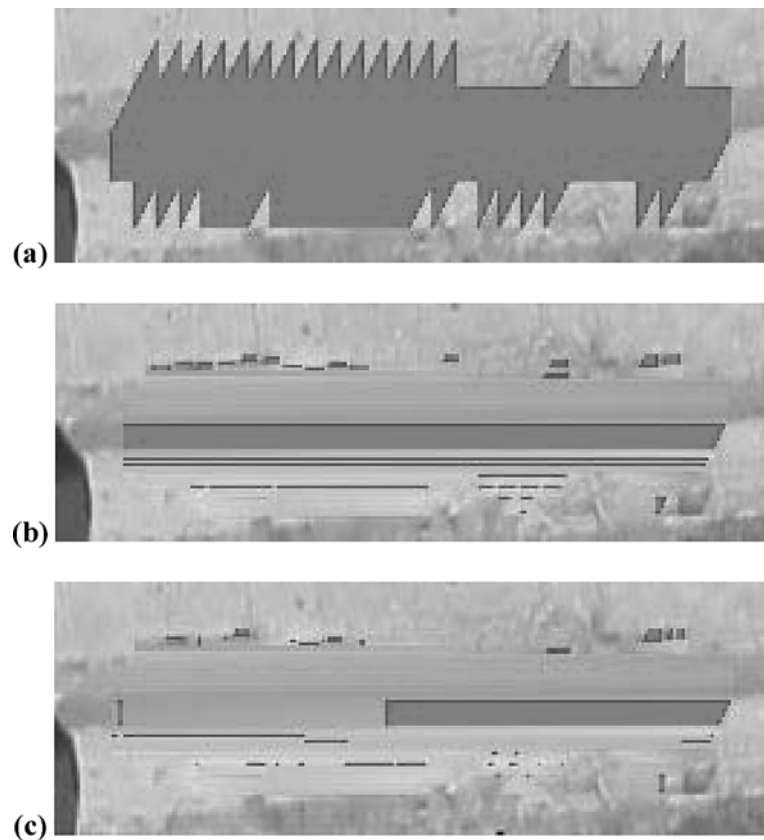


Figure 23. (a) part of a texture atlas with holes marked in red (b) after horizontal interpolation (c) after horizontal and vertical interpolation.

976 are stored in an array to be processed. A square win-
 977 dows w of size $(2M + 1) \times (2M + 1)$ pixels is centered
 978 at a hole pixel p , and the atlas is searched for a win-
 979 dows denoted by $bestmatch(w)$ which (a) has the same
 980 size as w , (b) does not contain more than 10% hole
 981 pixels, and (c) matches best with w . If the difference
 982 between w and $bestmatch(w)$ is below a threshold, the
 983 $bestmatch$ is classified as a good match to w and hole
 984 pixels of w are replaced with corresponding pixels in
 985 $bestmatch(w)$. The method is illustrated in Fig. 24.

986 For the method to work well, we need a suitable met-
 987 ric that accurately measures the perceptual difference
 988 between two windows, an efficient search process that
 989 finds the $bestmatch$ of a window w , a decision rule that
 990 classifies whether the $bestmatch$ found is good enough,
 991 and a strategy to deal with cases when the $bestmatch$
 992 of a window w is not a good match. In our proposed
 993 scheme, the difference between two windows consists
 of two components: (a) the sum of color differences

of corresponding pixels in the two windows, and (b) 994
 the number of outliers for the pair of windows. These 995
 components are weighted appropriately to compute the 996
 resulting difference. An efficient search is performed 997
 by constructing a hierarchy of Gaussian pyramids, and 998
 performing an exhaustive search at a coarse level to 999
 find a few good matches, which are then successively 1000
 refined at finer levels of the hierarchy. In cases when 1001
 no good match is found the window size is changed 1002
 adaptively. If a window of size $(2M + 1) \times (2M + 1)$ 1003
 does not result in a good match, the algorithm finds 1004
 the $bestmatch$ for a smaller window of size $(M + 1) \times$ 1005
 $(M + 1)$ and this process continues until the window 1006
 size becomes too small, in our case 9×9 pixels. If no 1007
 good match is found even after reducing the window 1008
 size, the hole pixels are filled by averaging the known 1009
 neighbors provided the pixel variance of the neighbors 1010
 is low; otherwise the colors of hole pixels are set to the 1011
 value of randomly chosen neighbors. 1012

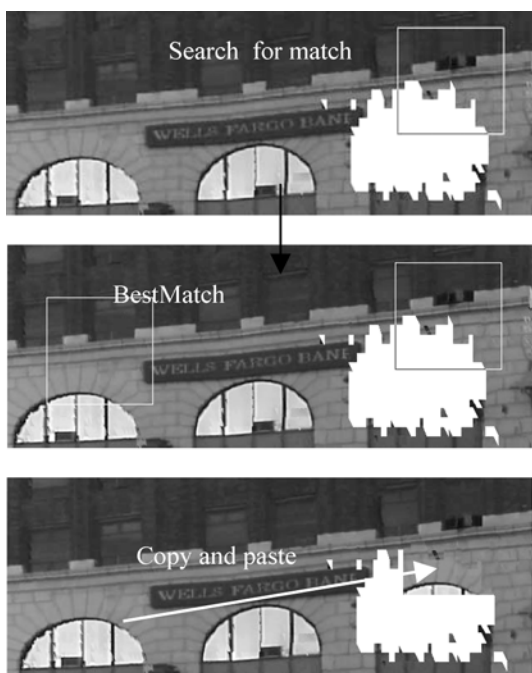


Figure 24. Illustrating the copy-paste method.

1013 8. Results

1014 We drove our equipped truck on a 6769 meters
1015 long path in downtown Berkeley, starting from Blake
1016 street through Telegraph avenue, and in loops around
1017 the downtown blocks. During this 24-minute-drive,
1018 we captured 107,082 vertical scans, consisting of
1019 14,973,064 scan points. For 11 minutes of driving time
1020 in the downtown area, we also recorded a total of 7,200
1021 camera images. Applying the described path splitting
1022 techniques, we divide the driven path into 73 segments,
1023 as shown in Fig. 25 overlaid with a road map. There is
1024 no need for further manual subdivision, even at Shat-
1025 tuck Avenue, where Berkeley's street grid structure is
1026 not preserved.

1027 8.1. Geometry Reconstruction

1028 For each of the 73 segments, we generate two meshes
1029 for comparison: the first mesh is obtained directly from
1030 the raw scans, and the second one from the depth im-
1031 age to which we have applied the postprocessing steps
1032 described in previous sections. For 12 out of the 73
1033 segments, additional 3D vertices derived from stereo
1034 vision techniques are available, and hence, sorting in



Figure 25. Entire path after split in quasi-linear segments.

these 3D points into the layers based on Section 5
1035 does fill some of the holes. For these specific holes, 1036
1037 we have compared the results based on stereo vision
1038 vertices with those based on interpolation alone as de-
1039 scribed in Section 6, and have found no substantial dif-
1040 ference; often the interpolated mesh vertices appear to
1041 be more visually appealing, as they are less noisy than
1042 the stereo vision based vertices. Figure 26(a) shows
1043 an example before processing, and Fig. 26(b) shows
1044 the tree holes completely filled in by stereo vision ver-
1045 tices. As seen, the outline of the original holes can
1046 still be recognized in Fig. 26(b), whereas the points
1047 generated by interpolation alone are almost indistin-
1048 guishable from the surrounding geometry, as seen in
1049 Fig. 26(c).

We have found our approach to work well in the
1050 downtown areas, where there are clear building struc-
1051 tures and few trees. However, in residential areas, 1052
1053 where the buildings are often almost completely hid-
1054 den behind trees, it is difficult to accurately estimate
1055 the geometry. As we do not have the ground truth
1056 to compare with, and as our main concern is the vi-
1057 sual quality of the generated model, we have manu-
1058 ally inspected the results and subjectively determined
1059 the degree to which the proposed postprocessing pro-
1060 cedures have improved the visual appearance. The
1061 evaluation results for all 73 segments before and af-
1062 ter postprocessing techniques described in this paper
1063 are shown in Table 1; the postprocessing does not uti-
1064 lize auxiliary 3D vertices from horizontal laser scan-
1065 ner or the camera. Even though 8% of all processed
1066 segments appear visually worse than the original, the
1067 overall quality of the facade models is significantly im-
1068 proved. The important downtown segments are in most

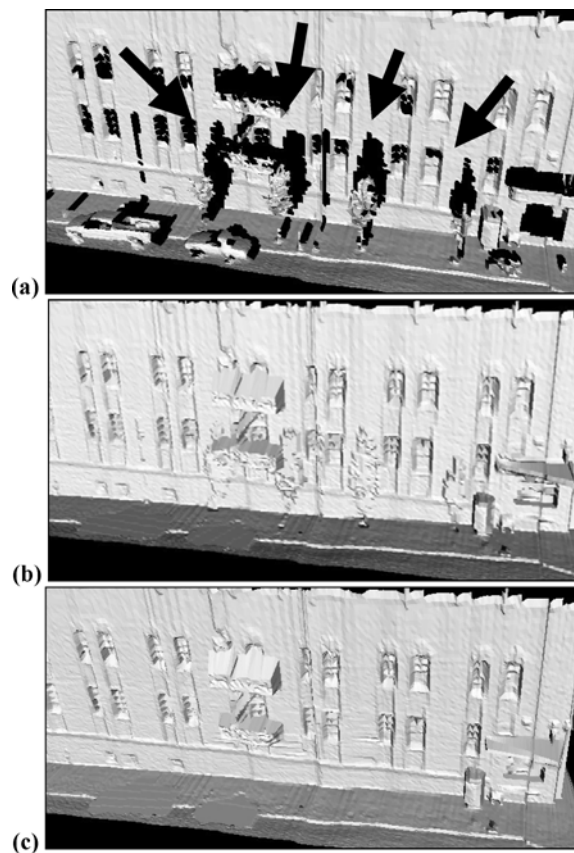


Figure 26. Hole filling. (a) Original mesh with holes behind occluding trees; (b) filled by sorting in additional 3D points using stereo vision; (c) filled by using the interpolation techniques of Section 6.

1069 cases ready to use and do not require further manual
1070 intervention.

1071 The few problematic segments all occur in residen-
1072 tial areas, consisting mainly of trees. The tree detection
1073 algorithm described in Section 5 classifies ten segments
1074 as “critical” in that too many trees are present; all six
1075 problematic segments corresponding to “worse” and
1076 “significantly worse” rows in Table 1 are among them,
1077 yet none of the improved segments in rows 1 and 2 are

Table 1. Visual comparison of the processed mesh vs. the original mesh for all 73 segments.

Significantly better	35	48%
Better	17	23%
Same	15	21%
Worse	5	7%
Significantly worse	1	1%
Total	73	100%

Table 2. Visual comparison of the processed mesh vs. the original mesh for the segments automatically classified as non-tree-areas.

Significantly better	35	56%
Better	17	27%
Same	11	17%
Worse	0	0%
Significantly worse	0	0%
Total	63	100%

1078 detected as critical. This is significant because it shows 1078
1079 that (a) all problematic segments correspond to regions 1079
1080 with a large number of trees, and (b) they can be suc- 1080
1081 cessfully detected and hence not be subjected to the 1081
1082 proposed steps. Table 2 shows the evaluation results if 1082
1083 only non-critical segments are processed. As seen, the 1083
1084 postprocessing steps described in this paper together 1084
1085 with the tree detection algorithm improve over 80% of 1085
1086 the segments, and never result in degradations for any 1086
1087 of the segments. 1087

1088 In Fig. 27 we show before and after examples, and 1088
1089 the corresponding classifications according to Tables 1 1089
1090 and 2. As seen, except for pair “f”, the proposed post- 1090
1091 processing steps result in visually pleasing models. Pair 1091
1092 f in Fig. 27 is classified by our tree detection algorithm 1092
1093 as critical, and hence, should be left “as is” rather than 1093
1094 processed. 1094

8.2. Texture Reconstruction 1095

1096 For 29 path segments or $3\frac{1}{2}$ city blocks, we recorded 1096
1097 camera images for texture mapping, and hence we re- 1097
1098 construct texture atlases as described in Section 7. Most 1098
1099 facade triangles which were occluded in the direct view 1099
1100 could be texture mapped from some other image with 1100
1101 an oblique view. Only 1.7% of the triangles were not 1101
1102 visible in any image, and therefore required texture 1102
1103 synthesis. 1103

1104 Figure 28 demonstrates our texture synthesis algo- 1104
1105 rithm. Figure 28(a) shows a closer view of the facade to- 1105
1106 gether with holes caused by occlusion from foreground 1106
1107 objects. The holes are marked in white. Figure 28(b) 1107
1108 shows the result using the hole filling technique de- 1108
1109 scribed in Section 7. As seen, the synthesized texture 1109
1110 improves the visual appearance of the model. For com- 1110
1111 parison purposes, Fig. 28 (c) shows the image resulting 1111
1112 from the inpainting algorithm described in Bertalmio 1112
1113 et al. (2000). A local algorithm such as inpainting only 1113
1114 uses the information contained in a thin band around the 1114

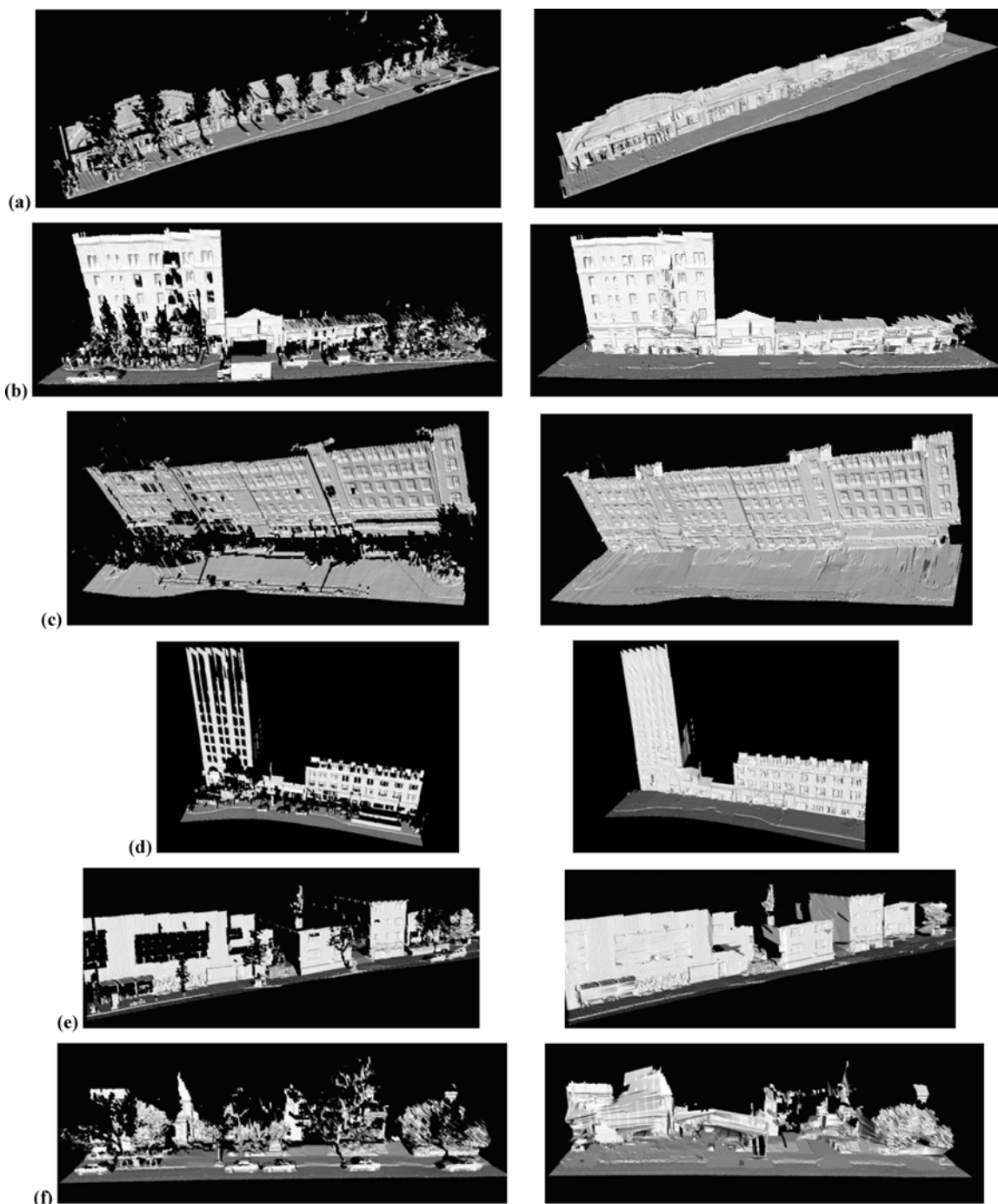


Figure 27. Generated meshes, left side original, right side after the proposed foreground removal and hole filling procedure. The classification for the visual impression is “significantly better” for the first four image pairs, “better” for pair e and “worse” for pair f.

1115 hole, and hence interpolation of surrounding boundary
1116 values cannot possibly reconstruct the window arch or
1117 the brick pattern on the wall. The copy-paste method on
1118 the other hand, is able to reconstruct the window arch

and brick pattern by copying and pasting from other
1119 parts of the image. 1120

In Fig. 29 we apply the texture atlas of Fig. 28 to the
1121 geometry shown in Fig. 27(d) and compare the model 1122

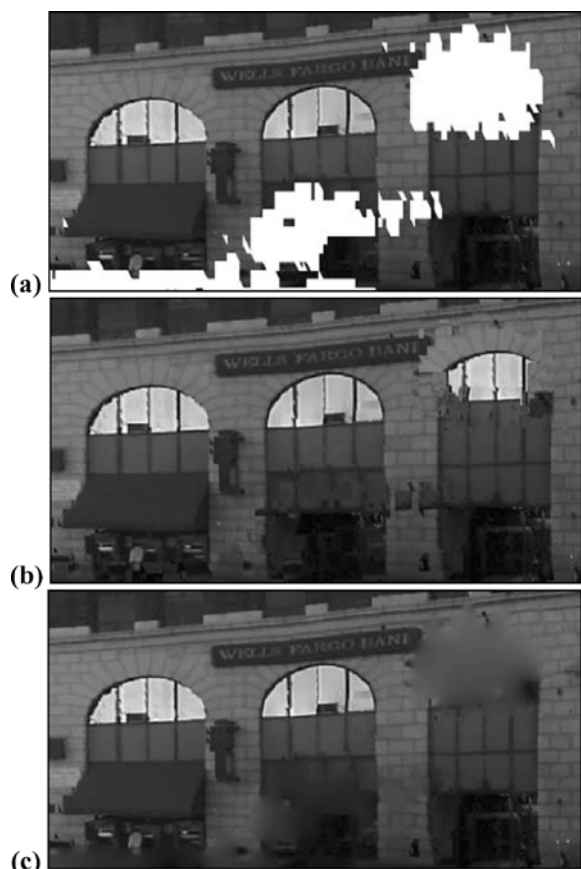


Figure 28. (a) part of texture atlas with holes marked in white; (b) hole filled atlas using the copy-paste method described in Section 7; (c) result of Inpainting.

1123 with and without the data processing algorithms de-
 1124 scribed in this paper, Figure 29(a) shows the model
 1125 without any processing, Fig. 29(b) the same model af-
 ter our proposed geometry processing, and Fig. 29(c)

the model after both geometry processing and texture
 synthesis. Note that in the large facade area occluded
 by the two trees on the left part of the original mesh,
 geometry has been filled in; while most of it could
 be texture mapped using oblique camera views, a few
 remaining triangles could only be textured via synthe-
 sis. As seen, the visual difference between the original
 mesh and the processed mesh is striking and appears
 to be even larger than in Fig. 27(d). This is because
 texture distracts the human eye from missing details
 and geometry imperfections introduced by hole filling
 algorithms. Finally, Fig. 30 shows the facade model for
 the entire $3\frac{1}{2}$ city blocks area.

8.3. Complexity and Processing Time 1139

Table 3 shows the processing time measured on a 2
 GHz Pentium 4 PC for the automated reconstruction of
 the $3\frac{1}{2}$ complete street blocks of downtown Berkeley
 shown in Fig. 30. Without the texture synthesis tech-
 nique of Section 7, thus leaving 1.7% of the triangles
 untextured, the processing time for the model recon-
 struction is 2 hours and 17 minutes. Due to the size
 of the texture, our texture synthesis algorithm is much
 slower, with processing time varying between <1 min
 and 8 hours per segment, depending on the number and
 the size of the holes. If quality is more important than
 processing speed, the entire model can be reconstructed
 with texture synthesis in about 23 hours.

Our approach is not only fast, but also automated:
 Besides the driving, which took 11 minutes for the
 model shown, the only manual step in our modeling
 approach is one mouse click needed to enter the ap-
 proximate starting position in the digital surface map
 for Monte-Carlo Localization, which is needed once

Table 3. Processing times for $3\frac{1}{2}$ downtown Berkeley blocks.

Processing Times for Automated Reconstruction on 2 GHz Pentium 4	
Data conversion	14 min
Path reconstruction based on scan matching and global correction with Monte Carlo Localization (with DSM and 5,000 particles)	70 min
Path segmentation	1 min
Geometry reconstruction	6 min
Texture mapping and atlas generation	27 min
Texture synthesis for atlas holes (including pixel-accurate image foreground removal)	20 h 51 min
Model optimization for rendering	19 min
Total model generation time without texture synthesis	2 h 17 min
Total model generation time with texture synthesis	23 h 08 min

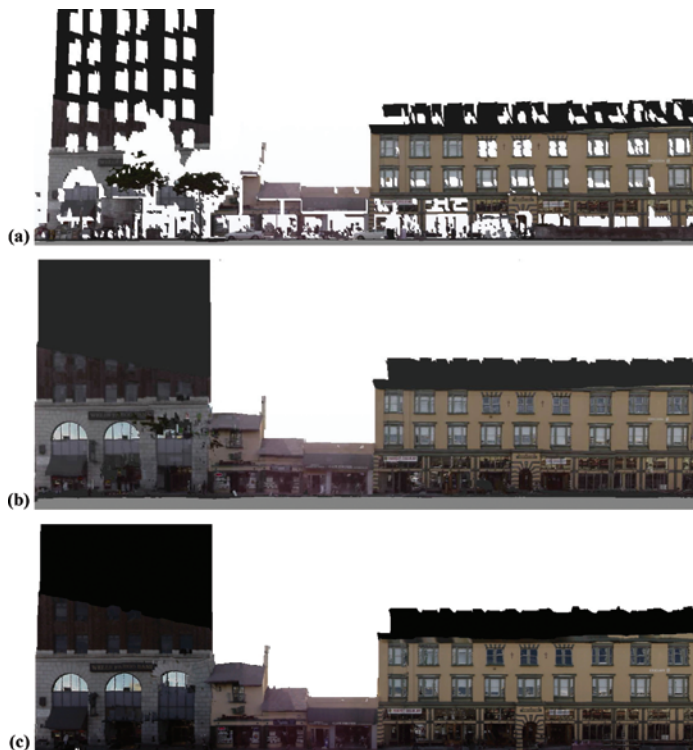


Figure 29. Textured facade mesh: (a) without any processing; (b) with geometry processing; and (c) with geometry processing, pixel-accurate foreground removal and texture synthesis.

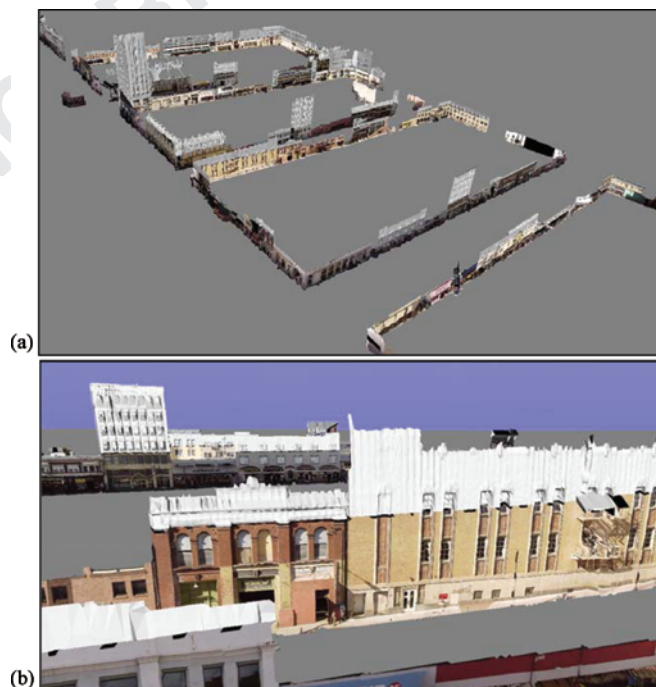


Figure 30. Reconstructed facade models: (a) overview; (b) close-up view.

1158 at the beginning of a model acquisition, and could be
1159 automated by using a low-cost GPS.

1160 8.4. Accuracy, Limitations, and Possible 1161 Failure Scenarios

1162 We have demonstrated that our approach is capable
1163 of reconstructing facade models for a large-scale ur-
1164 ban area. Since we do not have access to ground-truth
1165 geometry or texture data, it is difficult, if not impossi-
1166 ble, to assess the accuracy of the reconstructed models.
1167 However, the following observations can be made:

1168 The accuracy of the reconstructed model depends on
1169 (a) the accuracy of the raw scan points and (b) errors
1170 made during hole filling and mesh reconstruction. The
1171 vertical scan points have a basic random error of $\sigma_s =$
1172 ± 3.5 centimeters due to the scanner's measurement
1173 noise. As determined in Frueh (2002), the horizontal
1174 scan matching is accurate to within $\sigma_x = \sigma_y = 1$ cm
1175 for successive horizontal scans, which are on average
1176 about 1 meter apart. Thus, the relative position accu-
1177 racy for a path corresponding to N matched horizon-
1178 tal scans, or about N meters, is $\sigma_N = \sqrt{N \cdot (\sigma_x^2 + \sigma_y^2)}$.
1179 Therefore, the total uncertainty between 2 scan points
1180 p_1, p_2 recorded within N meters of driving can be esti-
1181 mated to $\sigma_{p_1, p_2} = \sqrt{N \cdot (\sigma_x^2 + \sigma_y^2) + 2\sigma_s^2}$. For exam-
1182 ple for a 10 meter wide facade, σ_{p_1, p_2} is 6.67 centimeter.
1183 Additionally, our Monte-Carlo-Localization-based ap-
1184 proach utilizes a DSM to correct drift-like global pose
1185 offsets in the vehicle's path by redistributing correction
1186 vectors among the relative motion estimates. By virtue
1187 of the parameters chosen in our Monte-Carlo localiza-
1188 tion, these correction vectors are designed to be of the
1189 same order of magnitude as σ_x . While the correction
1190 vectors are intended to compensate for errors made
1191 during the horizontal scan matching, they can add to
1192 the uncertainty due to inaccuracies in the DSM itself.
1193 Thus, our models are accurate, locally to about σ_{p_1, p_2} ,
1194 e.g. few centimeters, and globally to the accuracy of
1195 the DSM as a global map, e.g. one meter.

1196 Errors made during hole filling and mesh reconstruc-
1197 tion can be severe, depending on the scene and the
1198 amount of geometry that needs to be "invented". First,
1199 facades perpendicular to the driving direction or en-
1200 tirely occluded by large foreground objects are invis-
1201 ible to the laser scanner and hence not even result in a
1202 hole to be filled in—such structures do not appear in
1203 the model at all. Similarly, facades that are nearly all
1204 glass without surrounding solid walls would not pro-
1205 vide enough vertical scan points to be recognized as a

facade and would therefore not be reconstructed. Sec- 1206
ond, complicated facade objects such as fences, fire es- 1207
capes, or wires cannot be adequately reconstructed; due 1208
to their non-contiguous structure, corresponding scan 1209
points are classified as outliers and removed. Third, it 1210
is obvious that even a human operator can be wrong 1211
in filling a hole, since clues at the boundaries might be 1212
misleading; this is more so for an automated hole filling 1213
algorithm such as ours, which is based on interpolation 1214
and hence implicitly assumes a rather simple geometric 1215
structure. Forth, and most importantly, there are scenes 1216
for which a simple foreground/facade layer concept is 1217
not sufficient. Examples of these are more complex 1218
staged building structures with porches, pillars, oriels, 1219
or non-vertical walls, and residential areas with many 1220
trees. In these cases, our assumptions of Section 5 do 1221
not hold true any longer; using histogram analysis to 1222
separate the scan points into either foreground or fa- 1223
cades is inadequate and results in oddly reconstructed 1224
models as seen in Fig. 27(f). 1225

As a matter of fact, for complicated structures which 1226
differ substantially from a foreground/background sce- 1227
nario, our drive-by approach with one single vertical 1228
scanner does not provide enough data to successfully 1229
reconstruct a satisfactory model and hence is inappli- 1230
cable. Fortunately however, as demonstrated for down- 1231
town Berkeley, the street scenery in most downtown 1232
areas consists of a foreground/background composi- 1233
tion. As a solution to more complicated structures, mul- 1234
tiple vertical laser scanners could be mounted at dif- 1235
ferent orientations; similar to merging 3D scans taken 1236
from multiple viewpoints, these oblique scans could be 1237
used if direct scans are not sufficient. 1238

9. Conclusions 1239

We have proposed a method to reconstruct building fa- 1240
cade meshes from large laser surface scans and camera 1241
images, even in presence of occlusion. Future work will 1242
focus on using color and texture cues to verify filled- 1243
in geometry. Additionally, foreground objects could be 1244
classified and replaced by appropriate generics. 1245

Acknowledgment 1246

This work was sponsored by Army Research Office 1247
under contract DAAD19-00-1-0352. We wish to thank 1248
Sick, Inc. for their support. We also wish to thank John 1249
Flynn for providing the stereo vision results. 1250

1251 Note

- 1252** 1. The original image is more than 4 times larger in each dimension.
1253 This image is produced by subsampling the original image in
1254 a special way. Each white pixel corresponding to a foreground
1255 scan point in the original image is retained as a white pixel in the
1256 subsampled image. This gives a false impression that the density
1257 of foreground scan points is very high. On the other hand if the
1258 image is subsampled in the normal fashion, there would almost
 be no white pixels left in the subsampled image.

1259 References

- 1260** Ballester, C., Bertalmio, M., Caselles, V., Sapiro, G., and Verdera,
1261 J. 2001. Filling in by joint interpolation of vector fields and gray
1262 levels. In *IEEE Transactions on Image Processing*, pp. 1200–1211.
 Au: Pls. provide **1263** Ballester, C., Caselles, V., Verdera, J., Bertalmio, M., and Sapiro,
1264 G. A variational model for filling-in gray level and color images.
1265 In *Proc. 8th IEEE Int'l Conference on Computer Vision*, vol. 1,
1266 pp. 10–16.
1267 Bertalmio, M., Sapiro, G., Ballester, C., and Caselles, V. 2000.
1268 Image inpainting. In *Proc. SIGGRAPH 2000*, pp. 417–424.
1269 Chan, T. and Shen, J. 2001. Mathematical models for local
1270 nontexture inpaintings. *SIAM Journal on Applied Mathematics*
1271 62(3):1019–1043.
1272 Chang, N.L. and Zakhor, A. 1999. A multivalued representation for
1273 view synthesis. In *Proc. Int'l Conference on Image Processing*,
1274 Kobe, Japan, vol. 2, pp. 505–509.
1275 Curless, B. and Levoy, M. A volumetric method for building com-
1276 plex models from range images. In *SIGGRAPH*, New Orleans,
1277 pp. 303–312.
1278 Debevec, P.E., Taylor, C.J., and Malik, J. 1996. Modeling and ren-
1279 dering architecture from photographs. In *Proc. ACM SIGGRAPH*.
1280 Dick, A., Torr, P., Ruffe, S., and Cipolla, R. 2001. Combining single
1281 view recognition and multiple view stereo for architectural scenes.
1282 In *International Conference on Computer Vision*, Vancouver,
1283 Canada, pp. 268–274.
1284 Efros, A. and Freeman, W. 2001. Image quilting for texture synthesis
1285 and transfer. In *Proc. SIGGRAPH*, pp. 341–346.
1286 Fox, D., Thrun, S., Dellaert, F., and Burgard, W. 2000. Particle
1287 filters for mobile robot localization. In *Sequential Monte Carlo*
1288 *Methods in Practice*, A. Doucet, N. de Freitas, and N. Gordon
1289 (Eds.), Springer Verlag, New York.
1290 Frere, D., Vandekerckhove, J., Moons, T., and Van Gool, L. 1998.
1291 Automatic modelling and 3D reconstruction of urban build-
1292 ings from aerial imagery. In *IEEE International Geoscience and*
1293 *Remote Sensing Symposium Proceedings*, Seattle, pp. 2593–2596.
1294 Frueh, C. 2002. Automated 3D Model Generation for Urban
1295 Environments. Ph.D. Thesis, University of Karlsruhe.
1296 Frueh, C., Flynn, J., Foroosh, H., and Zakhor, A. 2001. Fast 3D model
1297 generation in urban environments. In *Workshop on the Conver-*
1298 *gence of Graphics, Vision, and Video (CGVV'01)*, Berkeley, USA.
 Frueh, C. and Zakhor, A. 2001a. Fast 3D model generation in urban
 environments. In *IEEE Conf. on Multisensor Fusion and Integra-*
tion for Intelligent Systems, Baden-Baden, Germany, pp. 165–170.
 Frueh, C. and Zakhor, A. 2001b. 3D model generation of cities using
 aerial photographs and ground level laser scans. In *Computer Vi-*
sion and Pattern Recognition, Hawaii, USA, vol. 2.2, pp. II-31-8.
 Frueh, C. and Zakhor, A. 2003. Constructing 3D city models by
 merging ground-based and airborne views. *IEEE Computer*
Graphics and Applications, Special Issue Nov/Dec, pp. 52–61.
 Garland, M. and Heckbert, P. 1997. Surface *Simplification Using*
Quadric Error Metrics. In *SIGGRAPH '97*, Los Angeles, pp. 209–216.
 Haala, N. and Brenner, C. 1997. Generation of 3D city models
 from airborne laser scanning data. In *Proc. EARSEL Workshop*
on LIDAR Remote Sensing on Land and Sea, Tallin, Estonia, pp. 105–112.
 Kim, Z., Huertas, A., and Nevatia, R. 2001. Automatic description
 of Buildings with complex rooftops from multiple images. In
Computer Vision and Pattern Recognition, Kauai, pp. 272–279.
 Koch, R., Pollefeys, M., and van Gool, L. 1999. Realistic 3D Scene
 modeling from uncalibrated image sequences. In *ICIP'99*, Kobe,
 Japan, Oct., pp. II: 500–504.
 Maas, H.-G. 2001. The suitability of airborne laser scanner data
 for automatic 3D object reconstruction. 3. In *Int'l Workshop on*
Automatic Extraction of Man-Made Objects, Ascona, Switzerland.
 Masnou, S. and Morel, J. 1998. Level-lines based disocclusion. In
5th IEEE Int'l Conference on Image Processing, pp. 259–263.
 Nitzberg, M., Mumford, D., and Shiota, T. 1993. *Filtering,*
Segmentation and Depth. Springer-Verlag: Berlin.
 Stamos, I. and Allen, P.K. 2002. Geometry and texture recov-
 ery of scenes of large scale. In *Computer Vision and Image*
Understanding (CVIU), 88(2):94–118.
 Stulp, F., Dell'Acqua, F., and Fisher, R.B. 2001. Reconstruction
 of surfaces behind occlusions in range images. In *Proc. 3rd Int.*
Conf. on 3-D Digital Imaging and Modeling, Montreal, Canada,
 pp. 232–239.
 Thrun, S., Burgard, W., and Fox, D. 2000. A real-time algorithm for
 mobile robot mapping with applications to multi-robot and 3D
 mapping. In *Proc. of International Conference on Robotics and*
Automation, San Francisco, vol. 1, pp. 321–328.
 Wang, X., Totaro, S., Taillardier, F., Hanson, A., and Teller, S. 2002.
 Recovering facade texture and microstructure from real-world
 images. In *Proc. 2nd International Workshop on Texture Analysis*
and Synthesis in Conjunction with European Conference on
Computer Vision, pp. 145–149.
 Zhao, H. and Shibasaki, R. 1999. A system for reconstructing urban
 3D objects using ground-based range and CCD images. In *Proc.*
of International Workshop on Urban Multi-Media/3D Mapping,
 Tokyo.
 Zhao, H. and Shibasaki, R. 2001. Reconstructing urban 3D model
 using vehicle-borne laser range scanners. In *Proc. of the 3rd*
International Conference on 3D Digital Imaging and Modeling,
 Quebec, Canada.